The Astrophysical Journal, 1002:64 (19pp), 2026 May 1 https://doi.org/10.3847/1538-4357/ae56e8
© 2026. The Author(s). Published by the American Astronomical Society.
OPEN ACCESS

Nowhere Left to Hide: Uncovering All of the Massive Young Embedded Star Clusters in the Antennae with JWST*

Rupali Chandar[1], Miranda Caputo[1], Paul Goudfrooij[2], Sean T. Linden[3], Angus Mok[4], Cory Whitcomb[1], Grant Donnelly[1], Florent Renaud[5,6], John-David T. Smith[1], Alberto Bolatto[7,8], Danny A. Dale[9], Sara Duval[1], Lindsey Hands[10], Ralf Klessen[11], Caroline Kuczek[1], Karin Sandstrom[10], Eva Schinnerer[12], and Fabian Walter[12]
[1] Ritter Astrophysical Research Center, University of Toledo, Toledo, OH 43606, USA; rupali.chandar@utoledo.edu
[2] Space Telescope Science Institute, 3700 San Martin Drive, Baltimore, MD 21218, USA
[3] Steward Observatory, University of Arizona, 933 N Cherry Avenue, Tucson, AZ 85721, USA
[4] OCAD University, Toronto, Ontario, M5T 1W1, Canada
[5] Observatoire Astronomique de Strasbourg, Université de Strasbourg, CNRS UMR 7550, F-67000 Strasbourg, France
[6] University of Strasbourg Institute for Advanced Study, 5 allée du Général Rouvillois, F-67083 Strasbourg, France
[7] Department of Astronomy, University of Maryland, College Park, MD 20742, USA
[8] Joint Space-Science Institute, University of Maryland, College Park, MD 20742, USA
[9] Department of Physics and Astronomy, University of Wyoming, Laramie, WY 82071, USA
[10] Department of Astronomy & Astrophysics, University of California, San Diego, 9500 Gilman Drive, San Diego, CA 92093, USA
[11] Universität Heidelberg, Zentrum für Astronomie, Institut für Theoretische Astrophysik, Albert-Ueberle-Str 2, D-69120 Heidelberg, Germany
[12] Max-Planck-Institut für Astronomie, Königstuhl 17, D-69117, Heidelberg, Germany
Received 2025 December 8; revised 2026 March 17; accepted 2026 March 20; published 2026 April 27

Abstract

The Antennae galaxies merger produces the brightest infrared emission of any galaxy within ≈20 Mpc, mostly from intense star formation taking place in supergiant molecular cloud complexes in the overlap region. Here, we present new, high-resolution NIRCam and MIRI images of the Antennae galaxies taken with the F150W, F187N, F335M, F360M, F410M, and F770W filters on JWST to search for the predicted but as-yet-undiscovered population of deeply embedded, optically obscured star clusters. We identify a population of 45 sources, 40 previously unknown, with high Brα/Hα and Paα/Hα flux ratios, which are likely very young clusters still embedded or just emerging from their natal cocoons, and estimate their age, extinction (A_V), and mass. We find that all are extremely young ($\lesssim$2.5 Myr), have A_V between 2 and 10 mag, and masses between $\approx 10^4$ and several $\times 10^6\,M_\odot$. We believe we have now uncovered all clusters with $M \gtrsim 3 \times 10^4\,M_\odot$ and $A_V \gtrsim 2$ mag in the Antennae. While our sample represents a small fraction (≈15%) of clusters younger than 3 Myr by number, it dominates the ionizing photon luminosity across the galaxy pair (≈60%). We find elevated H_2/polycyclic aromatic hydrocarbon ratios of the interstellar medium surrounding the most massive pair of embedded clusters, supporting the idea that merger-induced shock-heated gas plays an important role in the formation of extremely massive clusters.

Unified Astronomy Thesaurus concepts: Interacting galaxies (802)

Materials only available in the online version of record: machine-readable table

1. Introduction

The likely progenitors of globular star clusters (GCs) forming just ∼0.5–1 Gyr after the Big Bang have recently been discovered in James Webb Space Telescope (JWST) images of high-redshift galaxies (e.g., L. Mowla et al. 2022; E. Vanzella et al. 2022, 2023; A. Claeyssens et al. 2023; A. Adamo et al. 2024; M. Messa et al. 2024; P. Senchyna et al. 2024). This direct new evidence of massive cluster formation so early in cosmic history underscores the importance of understanding the physical processes that drive massive cluster formation and early evolution. In several systems, the estimated cluster masses are extremely high, reaching $\sim 10^6$–$10^7\,M_\odot$ (E. Vanzella et al. 2022, 2023; A. Adamo et al. 2024). Several of the parent galaxies show tidal features and morphological evidence of interactions, indications that processes commonly found in galaxy collisions almost certainly drive massive cluster formation (e.g., K. E. Whitaker et al. 2026). Because observations are currently limited to the high-mass end, the initial mass function (IMF) of GCs has not yet been measured directly.

The shape of the initial cluster mass function is a fundamental diagnostic of the star formation process on galaxy scales. GC masses reach $\approx 10^6\,M_\odot$ in Milky Way mass galaxies and have a steepening or cutoff at the high end (e.g., P. Goudfrooij et al. 2003; Y.-j. Peng et al. 2010; P. Goudfrooij & S. M. Fall 2016; G. De Lucia et al. 2024), which could either result from billions of years of evolution or have been imprinted at birth (e.g., S. M. Fall & M. J. Rees 1977; E. R. Capriotti & S. L. Hawley 1996; J. J. Kavelaars & D. A. Hanes 1997; S. M. Fall & Q. Zhang 2001; B. G. Elmegreen 2010). If imprinted at birth, such a cutoff would indicate a physical limit to the mass with which clusters can form. Unfortunately, the intense star formation needed to create such massive clusters is mostly

* This work is based on observations made with the NASA/ESA/CSA James Webb Space Telescope. The data were obtained from the Mikulski Archive for Space Telescopes at the Space Telescope Science Institute, which is operated by the Association of Universities for Research in Astronomy, Inc., under NASA contract NAS 5-03127 for JWST. These observations are associated with program #2581.

Original content from this work may be used under the terms of the Creative Commons Attribution 4.0 licence. Any further distribution of this work must maintain attribution to the author(s) and the title of the work, journal citation and DOI.

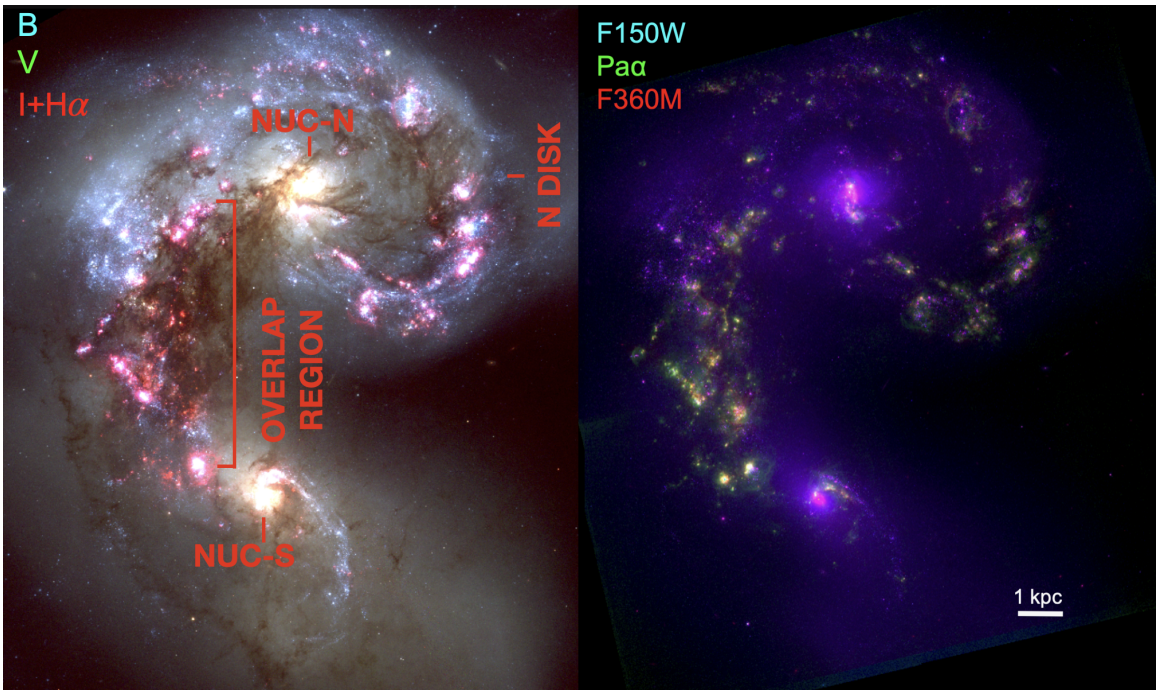

Figure 1. High-resolution color images of the merging Antennae galaxies are shown in the optical (left) from HST and in the infrared (right) from JWST in the indicated filters. The optical (B, V, I+Hα) filter combination gives a good view of dark dust lanes and warm ionized gas (pinkish red color) found throughout the Antennae and particularly in the overlap region, which is the region between and to the east of the two nuclei. The infrared (F150W, Paα, F360M) filter combination peers through this dust and allows us to identify optically obscured, very young star clusters that are still embedded in their natal ISM. North is up and east to the left, and the 1 kpc covers 10.″75 in each panel.

taking place in luminous infrared galaxies that are dust-obscured, distant, or both (e.g., A. Adamo et al. 2020; S. T. Linden et al. 2023). As the closest system forming clusters with masses $>10^6\,M_\odot$, the merging Antennae galaxies are ideal to assess the shape of the initial cluster mass function.

The overlap region in the Antennae, where the two progenitor spiral galaxies are merging together, and recent star formation is driving strong infrared emission (the strongest observed in any galaxy within ∼20 Mpc), is the closest system where extremely massive ($\approx10^6$–$10^7\,M_\odot$) clusters are forming. This region has intense star formation, a vast reservoir of cold gas organized into supergiant molecular cloud complexes (Y. Gao et al. 2001; C. D. Wilson et al. 2003), and many radio sources (S. G. Neff & J. S. Ulvestad 2000). Velocity maps from Atacama Large Millimeter/submillimeter Array (ALMA)/CO indicate that cloud–cloud collisions may play an important role in triggering the formation of massive clusters (K. Tsuge et al. 2021). A color image of the Antennae constructed from BVI+Hα filters taken by the Hubble Space Telescope (HST) is shown in the left panel of Figure 1. A number of very young, recently formed clusters are observed by their Hα emission (which makes them look pink) in the overlap region, but most of the area is dark because it is obscured by large amounts of dust. The high dust obscuration in the overlap region (I. F. Mirabel et al. 1998) and in other LIRGs suggests that optically based studies may be largely incomplete, and may miss as much as ≈60% of the recently formed ($\lesssim$6 Myr) cluster population (e.g., S. T. Linden et al. 2023). While extremely massive clusters are forming in other dusty, merger-driven (U)LIRGs, most of these systems are much further away, and the massive clusters tend to be significantly older (e.g., Arp 220, R. Chandar et al. 2023; NGC 7252, B. W. Miller et al. 1997; NGC 34 F. Schweizer & P. Seitzer 2007).

Our current understanding of the recent star and cluster formation histories in the Antennae relies mostly on optical studies with the HST (e.g., B. C. Whitmore et al. 1999, 2010; S. M. Fall & Q. Zhang 2001; S. M. Fall et al. 2005), and predictions from high-resolution (parsec-scale) hydrodynamical simulations of galaxy mergers (F. Renaud et al. 2015; H. Li et al. 2017). A number of works have concluded that most of the active star formation in the Antennae is embedded in thick layers of dust with high extinction $A_V \sim$ 30–70 mag, and is therefore invisible at optical (and possibly) near-infrared wavelengths (e.g., D. Kunze et al. 1996; I. F. Mirabel et al. 1998; S. G. Neff & J. S. Ulvestad 2000). If this is confirmed, current conclusions are based on an incomplete census of star clusters and may need to be revised. On the other hand, B. C. Whitmore & Q. Zhang (2002) concluded that most (≈85%) recently formed massive clusters have extinction values $A_V \lesssim 10$ mag and should be detected at optical wavelengths, at least in the I band.

The source WS80 is the best-known example of the embedded clusters we are searching for. It is the most massive ($>10^6\,M_\odot$), recently formed, highly extinguished cluster known in the Antennae (C. N. Herrera & F. Boulanger 2017). WS80 is the brightest source of thermal bremsstrahlung radiation at radio wavelengths in the Antennae, but is barely visible in a deep V-band HST image. If the mass function of very young (<3 Myr) clusters in the Antennae follows a power law with index $\beta \approx -2$ as found for the cluster population younger than 10 Myr (S. M. Fall & Q. Zhang 2001), there should be on the order of ≈50–100 WS80-like clusters with high extinction and masses greater than few $\times10^5 M_\odot$ forming in the overlap region, although very few such clusters have

Table 1
HST + JWST Observations of the Antennae

Instrument+ Camera	Filter Name	# Exposures	Total Exposure Time (s)	Proposal ID	VEGAMAG Zero-point[a]
HST/WFC3	F275W (NUV)	3	2610	14593	22.64 mag
HST/WFC3	F336W (*U*)	5	5534	11577	23.526 mag
HST/ACS	F435W (*B*)	3	1320	10188	25.766 mag
HST/WFC3	F555W (*V*)	2	1032	11577	25.843 mag
HST/ACS	F658N (Hα)	4	2300	10188	22.390 mag
HST/WFC3	F814W (*I*)	2	1032	11577	25.520 mag
JWST/NIRCam	F150W	24	7472	2581	1192.64 Jy
JWST/NIRCam	F187N (Paα)	12	3736	2581	779.34 Jy
JWST/NIRCam	F335M (3.3 μm PAH)	12	3736	2581	300.24 Jy
JWST/NIRCam	F360M	12	3736	2581	262.24 Jy
JWST/NIRCam	F410M (Brα)	12	3736	2581	208.45 Jy
JWST/MIRI	F770W (7.7 μm PAH)	4	244	2581	...

Note.
[a] Zero-points are from the instrument documentation available at www.stsci.edu.

been discovered to date. The main goal of this paper is to use new infrared images taken with the JWST of the merging Antennae galaxies to search for the predicted but as-yet-undiscovered population of deeply embedded/optically obscured massive ($\approx 10^4$–$10^6\,M_\odot$) clusters and to estimate their basic properties, i.e., age, extinction (A_V), and mass. In future work, newly discovered embedded sources will be combined with optically selected ones to create a complete census of obscured+unobscured clusters. We adopt a distance of 21.5 Mpc (distance modulus of $m - M = 31.66$; A. G. Riess et al. 2011) to the Antennae, which gives a physical scale of ≈ 104 pc arcsec^{-1}.

The rest of this paper is organized as follows. The new JWST observations and basic reduction are presented in Section 2, along with color images of the Antennae created from different optical–infrared filter combinations. In Section 3, we use maps of Brα/Hα and Paα/Hα flux ratios to select a new catalog of embedded cluster candidates in the Antennae, and in Section 4, we estimate the age, extinction, and mass for each cluster. Section 5 estimates the reddening and mass ranges of clusters that might still be missed in the JWST observations, determines the distribution of embedded cluster masses, and examines the local environment of the two most massive clusters to constrain formation mechanisms. We summarize the main results and discuss future plans in Section 6. The Appendix investigates the infrared emission from bright 6 cm sources from the S. G. Neff & J. S. Ulvestad (2000) catalog.

2. Observations of the Antennae

2.1. New JWST Images

Images of the Antennae galaxies were taken by JWST as part of program GO-2581 (PI: R. Chandar) in 2023 June using the F150W, F187N, F335M, F360M, and F410M filters on NIRCam and the F770M filter on MIRI. These filters cover stellar and dust continuum emission (F150W, F360M), hydrogen emission lines (Paα at 1.87 μm and Brα at 4.1 μm), and polycyclic aromatic hydrocarbon (PAH) features (3.3 and 7.7 μm). Basic information about the observations, including the number of dithered exposures and total photon collection time for each filter, is compiled in Table 1. All photometry in this work is in the VEGAMAG system.

With NIRCam, we use Module B, the FULL subarray, and an INTRAMODULEBOX primary dither pattern with four positions. At each primary dither position, we take three exposures using a "small-grid" subpixel dither pattern for a total of 12 exposures and 3736 s of photon collection time in the F187N, F335M, F360M, and F410M filters. The F150W filter was observed twice in this configuration, so it has 24 exposures and a total photon collection time of 7472 s. The SHALLOW4 readout pattern with one integration per exposure was used for all NIRCam observations. For our MIRI F770W observations, we use a four-point dither and the FASTR1 readout pattern, yielding a total photon collection time of 244 s.

We start with the uncalibrated raw ("uncal") files obtained from MAST and use Detector1Pipeline, which converts from "ramps" to "slopes" and applies basic detector-level corrections to the data, including flagging saturated pixels and correcting for chip persistence. We ran the Detector1Pipeline with the default parameters for most steps, except for the `ramp_fitting` step, for which we used `suppress_one_group = False` to avoid hard saturation for the brightest objects in the field. Stage 2 of the pipeline produces calibrated individual exposures. During this stage, the pixel coordinates are translated into WCS coordinates, which include a correction for geometric distortion. This stage also includes flat-fielding and background subtraction (the latter was only performed for the MIRI data).

Before combining the individual exposures, the individual, flatfielded NIRCam images are run through an algorithm that minimizes the effect of electronic $1/f$ noise. This algorithm, which is publicly available and described in JWST documentation,[13] masks pixels that have intensities $\gtrsim 3\sigma$ above the background, takes the median value of nonmasked pixels in each line in the slow readout direction and adjusts the level of each of those lines by subtracting the difference between those line medians and the overall median level of nonmasked pixels. Stage-3 combines individual tiles to produce a final, geometrically rectified mosaic of the Antennae in units of surface brightness (MJy sr^{-1}). The final redrizzling step

[13] https://jwst-docs.stsci.edu/known-issues/niriss-known-issues#NIRISSKnownIssues-1/fnoise

produces mosaics oriented with north pointing up and east to the left.

The standard mosaics produced by the Level-3 pipeline have good relative alignment between NIRCam tiles, but the alignment of the JWST images relative to other data with well-established absolute astrometry tends to be poorer, with offsets as large as $\sim 1''$ in some cases. Furthermore, there were nonnegligible offsets in pixel space between the Level-3 products of the different filters. For our final Stage-3 processing, we therefore performed additional corrections to improve the relative and absolute astrometry of the NIRCam and MIRI images using the `tweakreg` step of the pipeline. These corrections included: (i) creating a single reference star catalog to align all individual exposures, (ii) measuring "true" sky levels from custom sky regions; this was only important for the short-wavelength F150W and F187N filters, where the four individual detectors sample different regions within the full field of view. For this purpose, we use relative sky levels measured in the long-wavelength F360M image as a reference; (iii) matching the sky coordinates in the catalog to the Gaia DR3 reference frame, (iv) drizzling all Stage-3 products to a common celestial position for the reference pixel, and (v) adopting a common pixel scale and image size across all Stage-3 products. The final pixel scale of the images is $0\farcs031$ pix^{-1}.

2.2. Archival HST Images

The Antennae galaxies have been imaged by HST through several different programs over the years. In this work, we include archival observations in both broad- and narrowband filters covering the near-ultraviolet (NUV) and optical. We use observations taken with the WFC3/UVIS camera in the F275W/NUV (GO-14593, PI: N. Bastian), F336W/*U*, F555W/*V*, and F814W/*I* (GO-11577, PI: B. Whitmore) filters, and with the Advanced Camera for Surveys (ACS)/WFC camera in the F435W/*B*, and F658N/Hα filters (GO-10188; PI: B. Whitmore). Details of the HST observations, including the Proposal ID, number of exposures, and total exposure time, are compiled in Table 1.

Individual exposures are processed through the standard CALACS or CALWFC3 software, which performs initial data quality flagging, bias subtraction, gain correction, bias stripe removal, correction for CTE losses, dark current subtraction, flat-fielding, and photometric calibration. These individual files are aligned and drizzled to the common grid to create a single image per filter in counts s^{-1} using the DRIZZLEPAC software package. The WFC3 (ACS) images have a pixel scale of $0\farcs04$ pix^{-1} ($0\farcs05$ pix^{-1}) and are used for producing spectral energy distributions (SEDs).

2.3. Flux-calibrated, Continuum-subtracted Maps

The narrowband images contain both starlight and recombination line emission from ionized gas, and trace the locations of very recently formed massive stars and clusters. Because the optical light from the very youngest of these clusters is heavily extinguished because they are still embedded in their natal gas and dust, hydrogen recombination lines in the infrared (such as Paα and Brα) are well-suited to identify these young dusty objects. The 4.05 μm Brα line in particular is near the minimum in the Galactic extinction curve (K. D. Gordon et al. 2023).

We produce maps of hydrogen recombination lines by subtracting the stellar continuum from the narrow- and medium-band filters: F658N (Hα), F187N (Paα), and F410M (Brα). For Paα, we estimate the continuum level by interpolating between the F150W and F360M images (using a first-degree polynomial fit) to the central wavelength of the F187N filter. We then use several isolated, nonsaturated stars and intermediate-age clusters in the Antennae to determine the scale factor ($\sim$1.3) between our interpolated continuum image and the F187N line+continuum image. These sources do not have nebular or dust emission, so they should give a good measure of the stellar continuum in all filters. For the F410M filter, we adopt the nearby F360M image as our "continuum" and scale it based on the same line-free sources described above. This filter is the closest one in wavelength that does not contain significant contributions from dust or recombination line emission. To create Hα line maps, we adopt a scaled (by a factor of 0.64) F814W filter as the continuum and subtract this from the F658N image. All continuum-subtracted images are in physical flux density units of erg s^{-1} cm^{-2} Hz^{-1}. These continuum-subtracted Hα, Paα, and Brα maps will be used to search for recently formed, embedded clusters.

2.4. Spitzer Mid-infrared Spectroscopy

Most of the Antennae, including the interaction region, was observed by the Infrared Spectrograph (IRS) on Spitzer as part of program 21 (PI: J.R. Houck). The observations span the wavelength range 5.2–14.7 μm with a scale of $\sim 1\farcs8$ pix^{-1} and from 14.2 to 38.4 μm at $\sim 5\farcs1$ pix^{-1}. Previously, B. R. Brandl et al. (2009) extracted and analyzed the spectra for six bright infrared peaks and the two galactic nuclei from these observations.

Spitzer/IRS data cubes are created as part of a uniform reduction of all low spectral resolution IRS mapping programs, which includes hundreds of galaxies, by the Spitzer/IRS Mapping Legacy Archive (SIMLA) project (G. P. Donnelly et al. 2025). The SIMLA pipeline leveraged off-source observations from the entire IRS archive to create custom backgrounds for each spectral map, resulting in significantly reduced noise in the extracted spectra. In this work, we measure the H_2/PAH ratio from the Spitzer spectra in a few special locations in the Antennae, and leave a more detailed investigation of the full region and rich spectral features to future work.

2.5. An Infrared View of Optically Dark Regions

Figure 1 contrasts the Antennae in optical (left panel) and infrared light (right panel). The north and south nuclei, partially intact northern disk, and dusty overlap region (the region to the east between the two galaxy nuclei) are all clearly seen in the optical filter combination of *B*, *V*, *I*+Hα displayed in the left panel. This filter combination highlights the dark dust lanes found throughout the Antennae, particularly in the overlap region, where some areas appear fully dark with little Hα emission from recently formed star clusters. The infrared (F150W, Paα, F360M) filter combination in the right panel minimizes this obscuration and reveals sites where star formation is (and is not) taking place. With the new JWST images, we can essentially see all of the massive clusters forming in the Antennae.

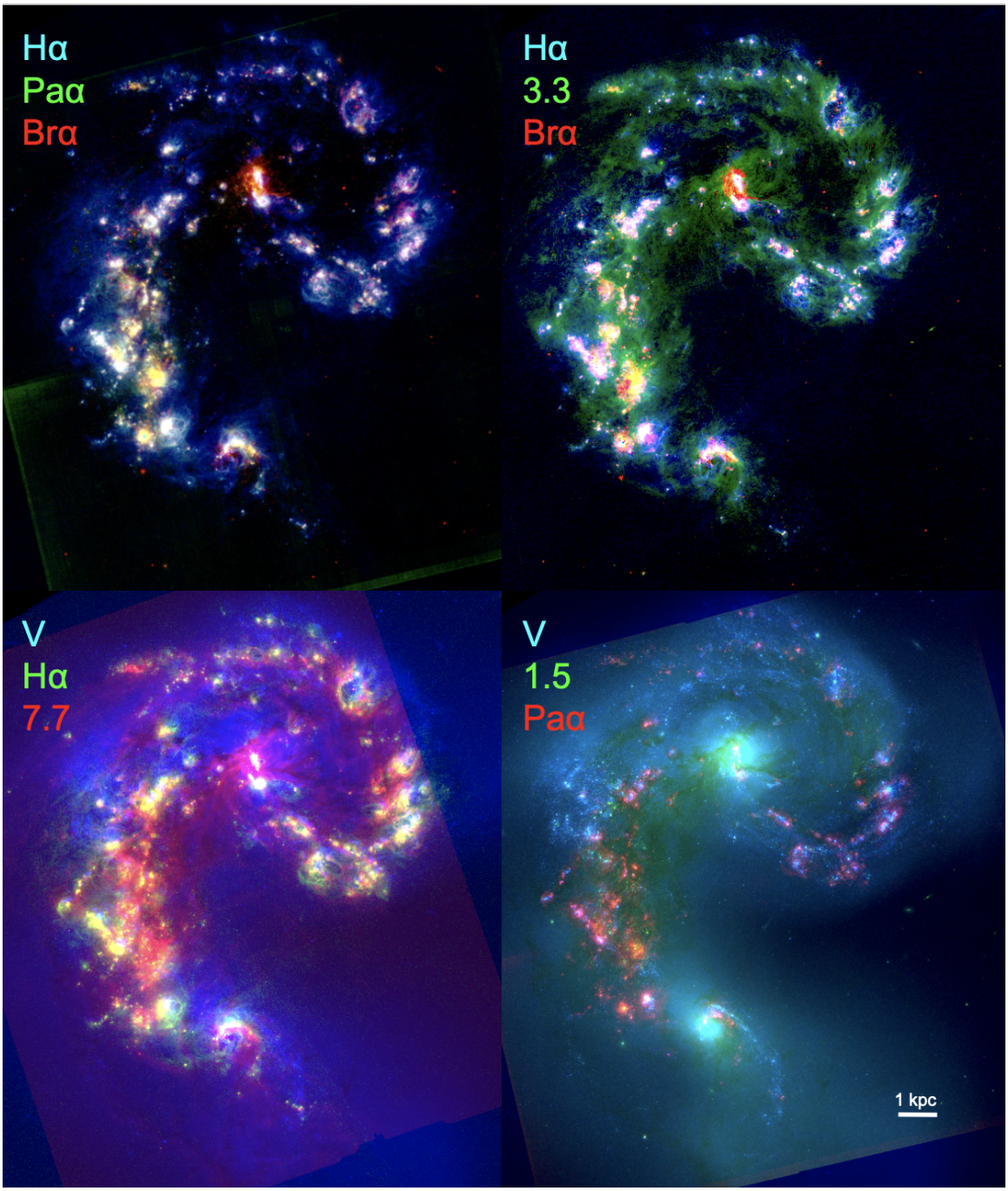

Figure 2. Color images of the Antennae are shown in four different filter combinations, as indicated in each panel. Maps which include Hα, Paα, Brα, and 3.3 μm emission have all been continuum-subtracted as described in Section 2.3.

In Figure 2, we show different combinations of JWST+HST filters to highlight different aspects of this iconic system.

1. *Top left*. This image combines the continuum-subtracted Hα (blue), Paα (green), and Brα (red) maps to highlight warm ionized gas. For the most part, this emission traces natal gas ionized by massive stars within recently formed star clusters. Warm ionized gas is observed throughout the Antennae, from the northern disk, throughout the overlap region, and near the southern nucleus. The gas shows a range of colors, indicating a range of extinction, with the most highly extinguished regions found mostly in the overlap region. The latter appear yellow since they are dominated by Paα emission and their inferred extinctions lie between 4.5 and 15 mag.
2. *Top right*. An image of 3.3 μm emitting dust grains replaces the continuum-subtracted Paα image from the top-left panel (in green). Most of the green in this image, where the 3.3 μm PAH emission dominates over Hα and Brα, is diffuse and extends away from regions of ionized gas. Strong 3.3 μm emission is also cospatial with many (but not all) shells and bubbles around H II regions, as also observed in a sample of PHANGS galaxies (M. J. Rodríguez et al. 2025). We will study the association between PAH emission and young stellar clusters in the Antennae in an upcoming paper.

3. *Bottom left*. This color composite is created from the V (blue), Hα (green), and 7.7 μm PAH band images. Like the previous image, there is a significant amount of diffusely distributed PAH emission, now seen in red. This image also reveals an interesting "bubble" in the northern disk, where the 7.7 μm emission appears to fall just outside of an Hα shell. This bubble is reminiscent of the "Phantom Void," a large, feedback-driven ∼kilo-parsec-scale bubble observed in PAH emission in the spiral galaxy NGC 628 (A. T. Barnes et al. 2023).
4. *Bottom right*. The combination of the V band (blue), F150W (green), and continuum-subtracted Paα (red) filters highlights differences in the warm ionized gas properties in the northern disk, which are a dark pink color, with those in the overlap region, which are more of an orange–red due to their higher extinction. Many blue, slightly older (by a few Myr) clusters are also observed in the northern disk.

3. A New Catalog of Very Young, Embedded Clusters in the Antennae

3.1. Cluster Selection Based on Hydrogen Recombination Line Ratios

Recently formed star clusters are typically still surrounded by their parental cloud of gas and dust, which makes their emission difficult to detect at optical wavelengths but easier at longer wavelengths. Because the intrinsic flux ratios for Hα/Brα and Hα/Paα are 36.679 and 8.584, respectively (D. G. Hummer & P. J. Storey 1987), Hα will be stronger than Paα and Brα in H II regions with nebular extinction $A_V \lesssim 4.5$ mag, Paα will be strongest for sources with $A_V \approx 4.5$ to ≈15 mag, and Brα will be strongest for sources with $A_V \gtrsim 15$ mag.[14] Note that the D. Calzetti et al. (2000) law finds that the nebular reddening is ≈2.27 times higher than the reddening experienced by stellar emission. In this section, we use our high-resolution maps of hydrogen recombination line emission in Hα, Paα, and Brα to identify embedded star clusters in the Antennae.

Maps of Brα/Hα and Paα/Hα flux ratios are ideal for identifying sources with high nebular extinction (e.g., B. R. Brandl et al. 2012; M. Messa et al. 2021; G. B. Graham et al. 2025). As a guide to the specific flux ratios to use from our maps, we examine the measured ratios for WS80 and its companion, the latter being another very young, massive cluster with moderate reddening, which was first identified by V. C. Rubin et al. (1970). Images of this cluster pair are shown in Figure 3 from 0.275 μm through 7.7 μm, with WS80 identified by the cyan cross. WS80 is not detected in the NUV, U, or B filters, is very faint in V, Hα, and I, becomes progressively brighter toward longer wavelengths, and by ≈1.5 μm is the brightest source in the Antennae. By contrast, its neighbor is the brightest source (excluding the galactic nuclei) in the NUV (F275W) and U (F336W) bands, and remains bright over all plotted wavelengths, including Paα and Brα. WS80 and its companion are among the brightest sources in the Paα/Hα line ratio map shown in the right panel of Figure 4, and WS80 is the brightest source in both maps.

[14] These estimates assume Case B recombination for a typical electron temperature of 10,000 K, electron density 1×10^4, and a Milky Way–like attenuation curve with $R_V = 3.1$.

Based on the observed ratios for WS80 and its neighbor, we require a candidate embedded cluster to have (at least) one pixel with Paα/H$\alpha \geqslant 5$ or Brα/H$\alpha \geqslant 1$, or to have at least three contiguous pixels with Paα/H$\alpha \geqslant 3$ or Brα/H$\alpha \geqslant 0.6$. An initial list of embedded cluster candidates that satisfied these criteria is selected automatically from the flux ratio maps, followed by careful visual inspection of each candidate in both maps. Two additional criteria were imposed on sources that satisfied these line ratios: (i) the source must have similar morphology in the Paα/Hα and Brα/Hα ratio maps (this step eliminated a number of point sources with imperfect continuum subtraction); and (ii) the source must be broader than the point-spread function (PSF) at 3.6 μm (more below).

We identify 45 candidate embedded clusters that satisfy our selection criteria and list their coordinates in Table 2. All have Paα and Brα emission; we did not discover any sources with Brα but no Paα emission. Not surprisingly, most of the embedded clusters (28/45 or ≈60%) are found in the overlap region between the two galaxies. Approximately 15% (6/45) are in the southern galaxy (all but one in the optically dark star-forming arc around the nucleus), while ≈25% (11/45) are forming in the disk of the northern galaxy. We do not identify any embedded cluster candidate in the "Firecracker" (B. C. Whitmore et al. 2014), despite high flux ratios (Brα/H$\alpha > 1$) throughout the region (see Figure 4). The Firecracker is a well-studied, infrared-bright region located north and slightly west of WS80 (see Figure 4) with no known star or cluster formation (B. C. Whitmore et al. 2014; K. E. Johnson et al. 2015; M. K. Finn et al. 2019, although see C. N. Herrera & F. Boulanger 2017) for a different view, lending confidence to our selection criteria.

As mentioned earlier, embedded cluster candidates are selected to be broader than the PSF in the F360M filter, since many are faint at 1.5 μm but brighter at 3.6 μm. Following D. A. Thilker et al. (2022), we measure a set of multiple concentration indices (MCI) to determine if a source is broader than the PSF, where a concentration index is simply the difference in magnitude measured in two apertures. MCI is defined for pairs of radii (a, b), (b, c), and (c, d) as the average: $\mathrm{MCI} = \overline{[\mathrm{NCI}(a, b), \mathrm{NCI}(b, c), \mathrm{NCI}(c, d)]}$, where NCI is the concentration index "normalized" relative to a fiducial cluster. We calculate an inner and outer value using radii of 1.0, 1.5, 2.0, and 2.5 pixels (2.5, 3.0, 4.0, 5.0 pixels) as a, b, c, d for $\mathrm{MCI_{in}}$ ($\mathrm{MCI_{out}}$). The results in Figure 5 show that the embedded cluster candidates have higher MCI values than a hand-selected training set of stars, indicating they are more extended than the PSF. These overlap with the structural parameters measured for a new catalog of F150W-selected clusters, although the embedded clusters tend to have somewhat less extended outskirts than older clusters (i.e., they have slightly lower $\mathrm{MCI_{out}}$ for a given $\mathrm{MCI_{in}}$), consistent with expectations that these very young clusters will expand as they age; R. Chandar et al. (2016).

We emphasize that our 45 embedded cluster candidates, identified by the red circles in Figure 6, are not the full sample of clusters in the Antennae, just some of the youngest and most extinguished ones. In an upcoming work (M. Caputo et al.), we will present a new catalog of star clusters selected to be broader than the PSF in the F150W JWST image. This catalog includes clusters that are both obscured and unobscured in V-band images taken with HST. Figure 5 shows that the embedded clusters selected here (black circles) have similar

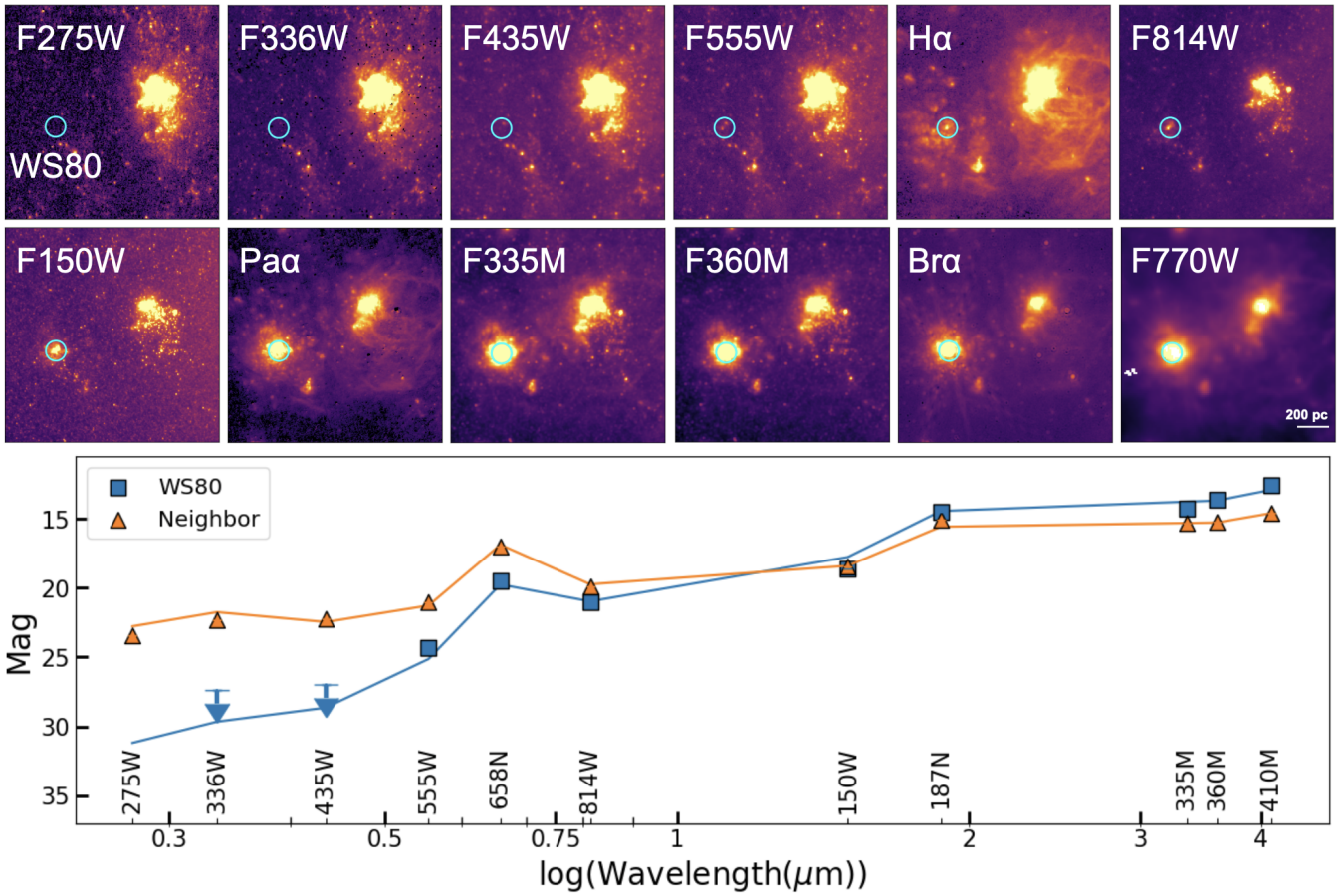

Figure 3. The embedded, extremely massive star cluster WS80 (identified by the cyan circle) and its nearby companion (also a massive young cluster but with more moderate extinction) are shown in 12 HST+JWST filters, starting from the NUV in the upper left through the JWST/F770W filter in the lower right. Each filter shows a 12.″5 × 12.″5 region around the clusters. WS80 is not seen in the NUV, *U*, or *B* filters but can be observed as a faint source in the *V*, Hα, and *I* filters through the cyan cross. WS80 gets brighter and brighter toward longer wavelengths, and by 3.3 μm is the brightest source in the Antennae. By contrast, its companion cluster is bright in all 12 filters. The lower panel shows the measured photometry for the two clusters, with the best-fit SED models overplotted (see Section 4.1).

structural parameters to the 1.5 μm selected clusters (gray circles).

3.2. An Assessment of Different Infrared Tracers for Identifying Embedded Clusters

A number of recent works have used different combinations of high-resolution Paα, Brα, and 3.3 μm JWST imaging to identify embedded star clusters in nearby galaxies (e.g., M. J. Rodríguez et al. 2023, 2025; B. Gregg et al. 2024; G. B. Graham et al. 2025; A. Knutas et al. 2025). The FEAST collaboration has defined embedded candidates (designated as emerging young star clusters or "eYSCI") as sources with a Brα and 3.3 μm PAH peak within 4 pixels (∼0.″16) of a Paα emission peak. Their selection results in 737 sources in the spiral galaxy NGC 628 that have an average reddening $E(B-V) \sim 0.5$ mag or extinction $A_V \sim 1.5$ mag (B. Gregg et al. 2024), and in 946 sources in M83 with a median $E(B-V) \sim 0.8$ mag or $A_V \sim 2.5$ mag (A. Knutas et al. 2025) for a Milky Way–like extinction curve. They suggest that clusters with peaked Paα and Brα emission but diffuse (and weaker) 3.3 μm PAH emission (designated "eYSCII") are somewhat older (by ≈1–2 Myr) than the eYSCI sources.

As part of the PHANGs collaboration, M. J. Rodríguez et al. (2023, 2025) selected embedded cluster candidates that may be missed in optically selected samples in spiral galaxies through their 3.3 μm PAH emission. While they did not estimate extinction, they found that ∼40% of the 3.3 μm sources detected in NGC 7469 were not selected as clusters at optical wavelengths (M. J. Rodríguez et al. 2023).

While identifying embedded cluster candidates in the Antennae based on the selection criteria used by the FEAST and PHANGS collaborations is beyond the scope of this paper, we offer a qualitative assessment of the source catalogs that would result from applying these selection criteria to our Antennae data. We can easily count a few hundred sources with overlapping Paα, Brα, and 3.3 μm emission, including our embedded clusters. These sources have significantly lower Brα/Hα and Paα/Hα ratios than the thresholds adopted here, and therefore almost certainly experience less extinction. Most of these sources are identifiable in the HST *V*-band image, supporting the idea that they are young, line-emitting clusters with low extinction A_V. We conclude that combinations of Paα (Brα) and 3.3 μm emission provide an excellent way to identify very young clusters regardless of the amount of extinction they experience. The method used here of identifying clusters based on their high Paα/Hα and Brα/Hα line ratios preferentially selects the subset of very young clusters with higher extinction, most of which are not identifiable as clusters from their broadband optical emission.

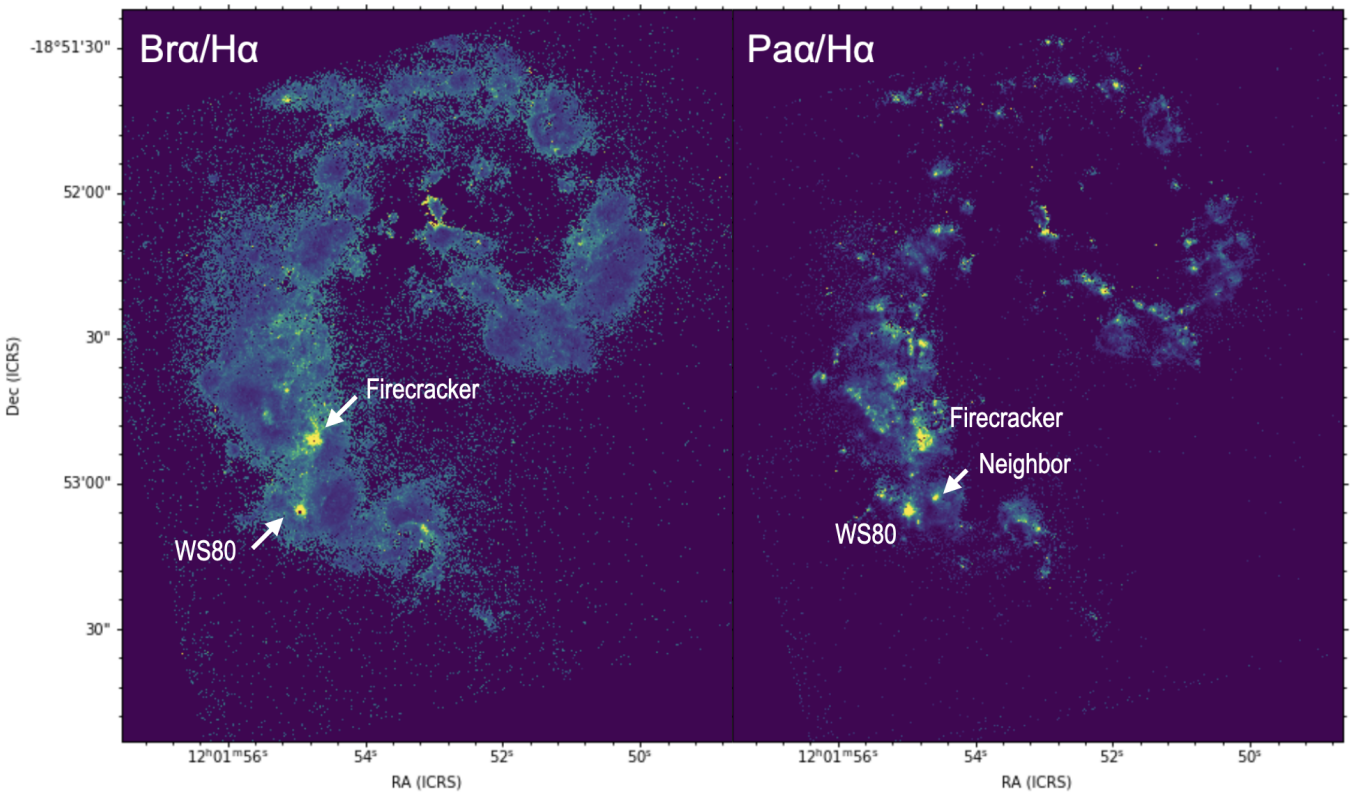

Figure 4. Brα/Hα (left) and Paα/Hα flux ratio maps used to identify embedded clusters from their high extinction. WS80 is the brightest source in both images, while its neighbor, which is known to have lower extinction, is only bright in Paα/Hα. The Firecracker is bright in both ratio maps, but star formation has yet to take place in this region (it may in the near future).

4. Deriving the Properties of Embedded Clusters

4.1. SED Fitting

In this section, we estimate the age, reddening, and mass of each embedded cluster by fitting its observed SED with predictions from cluster evolution models that extend to infrared wavelengths and include emission from both stars and interstellar medium (ISM).

In preparation for SED fitting, we perform aperture photometry using the PHOTUTILS package (L. Bradley et al. 2024) using a measurement radius of 0.″155 uniformly across all HST and JWST/NIRCam images. The sky background is measured in an annulus with radii between 0.″50 and 0.″62 from the source centers. The shape of the SED is affected by the age of the cluster stars and the amount and condition of the ISM, and its normalization is tied to cluster mass. We estimate the amount of light missing in the aperture by measuring the magnitude difference of each source between 0.″155 and 0.″465 in the F360W filter (difference between 5 and 15 pixel radii). The median aperture correction is −1.29 mag, and the values measured for each cluster are listed in column (7) of Table 2. In a future paper, we will present size-dependent aperture corrections for a full catalog of optically obscured+unobscured star clusters in the Antennae, but curves of growth for the embedded clusters suggest that the simple approach adopted here gives results within ≈25% of the total flux.

For the SED fitting, we adopt the flexible stellar population synthesis (FSPS) code (C. Conroy et al. 2009, 2010) to determine the best-fit combination of age and reddening. The models include dust extinction and emission, nebular line and continuum emission, and circumstellar emission around AGB stars. Full details of the fitting procedure will be provided along with the total sample of clusters at all ages in an upcoming work (M. Caputo et al. 2026, in preparation); here, we summarize the basic assumptions and method. We use the Python package PYTHON-FSPS (B. Johnson et al. 2024) to create integrated-light spectra of single-age stellar populations with solar metallicity and a P. Kroupa (2001) IMF. The synthetic cluster spectra are placed at the redshift of the Antennae ($z = 0.0055$, see NED[15]). For the age range, we choose $5.5 \leqslant \log(\mathrm{age/yr}) \leqslant 10.2$ in steps of 0.1 dex. For extinction, we allow the range $0.0 \leqslant A_V \leqslant 80.0$ mag in steps of 0.1 mag, assuming a Milky Way–like value for R_V of 3.1, but find very similar age–A_V results if we adopt the D. Calzetti et al. (2010) extinction law instead. We select models from the PARSEC isochrone family (A. Bressan et al. 2012; C. T. Nguyen et al. 2022) and the MILES spectral library (P. Sánchez-Blázquez et al. 2006; A. Vazdekis et al. 2010, 2016).

To create predicted cluster photometry, the spectra are integrated over the HST/ACS, HST/WFC3, and JWST/NIRCam passbands by incorporating throughput tables downloaded from the STScI website into the FSPS package. Predicted magnitudes are derived based on an assumed distance to the Antennae of $m - M = 31.66$ (A. G. Riess et al. 2011).

The best-fit age and reddening for each cluster are determined as follows. For each cluster, we first normalize the model magnitudes by subtracting the weighted mean offset between the model grid and observed cluster magnitudes,

[15] https://ned.ipac.caltech.edu

Table 2
Catalog of Embedded Star Cluster Candidates

Source[1] ID	R.A. (J2000)	Decl. (J2000)	Age [log (τ/yr)]	A_V (mag)	Mass [log ($M/M_\odot$)]	apcorr[a] (mag)	CrossID
1	12:01:52.2400	−18:53:27.9597	$5.8^{+0.5}_{-0.5}$	$3.4^{+0.8}_{-0.6}$	4.4 ± 0.3	−1.2	…
2	12:01:52.9578	−18:53:15.4353	$5.7^{+0.55}_{-0.4}$	$2.4^{+0.6}_{-0.6}$	4.3 ± 0.3	−0.7	…
3	12:01:53.0859	−18:53:9.81857	$6.4^{+0.74}_{-0.86}$	$4.8^{+0.92}_{-0.88}$	4.8 ± 0.7	−1.7	…
4	12:01:53.1226	−18:53:9.77737	$6.6^{+1.6}_{-0.7}$	$6.6^{+2.4}_{-2.0}$	5.1 ± 1.2	−1.8	possibly NU1-3
5	12:01:53.1592	−18:53:8.80920	$5.8^{+0.5}_{-0.5}$	$6.6^{+2.4}_{-2.19}$	5.0 ± 0.8	−1.4	…
6	12:01:53.2983	−18:53:8.12256	$6.4^{+0.62}_{-0.8}$	$5.2^{+0.4}_{-0.59}$	5.0 ± 0.7	−1.6	…
7	12:01:54.1956	−18:53:8.95340	$6.0^{+0.65}_{-0.71}$	$2.2^{+0.61}_{-0.53}$	4.5 ± 0.2	−0.7	…
8	12:01:55.0378	−18:53:11.3635	$6.35^{+1.84}_{-0.94}$	$2.2^{+0.8}_{-0.8}$	4.3 ± 0.3	−1.4	…
9	12:01:54.9536	−18:53:5.96649	$6.3^{+0.63}_{-0.8}$	$9.2^{+1.36}_{-1.16}$	6.5 ± 0.3	−0.9	WS80, NU2-1
10	12:01:54.8254	−18:53:7.76550	$5.7^{+0.5}_{-0.4}$	$3.4^{+1.0}_{-0.8}$	5.0 ± 0.8	−1.5	…
11	12:01:54.7742	−18:53:6.28922	$6.0^{+1.64}_{-0.64}$	$3.4^{+4.04}_{-2.6}$	4.5 ± 0.4	−1.3	…
12	12:01:54.6826	−18:53:5.67810	$5.7^{+0.5}_{-0.4}$	$3.2^{+0.6}_{-0.6}$	4.3 ± 0.3	−1.0	…
13	12:01:54.5911	−18:53:3.01392	$6.4^{+0.42}_{-0.11}$	$3.4^{+0.21}_{-0.21}$	5.9 ± 0.5	−1.3	Companion, NU2-6
14	12:01:55.3564	−18:53:2.64999	$5.7^{+0.5}_{-0.4}$	$2.4^{+0.6}_{-0.6}$	4.9 ± 0.3	−1.4	…
15	12:01:55.2100	−18:53:3.19244	$5.8^{+0.5}_{-0.5}$	$3.0^{+0.8}_{-1.0}$	4.3 ± 0.4	−1.1	…
16	12:01:55.4407	−18:53:0.741119	$5.85^{+0.75}_{-0.55}$	$3.6^{+1.2}_{-1.0}$	4.1 ± 0.4	−0.9	…
17	12:01:55.3564	−18:53:1.86035	$5.8^{+0.6}_{-0.5}$	$4.2^{+1.4}_{-1.4}$	4.7 ± 0.5	−1.1	…
18	12:01:55.3088	−18:53:1.50330	$6.0^{+2.23}_{-0.63}$	$4.2^{+2.44}_{-2.2}$	4.2 ± 0.7	−1.4	…
19	12:01:55.2136	−18:53:1.24924	$5.8^{+0.6}_{-0.5}$	$3.0^{+1.2}_{-1.0}$	4.1 ± 0.4	−1.1	…
20	12:01:54.9280	−18:52:58.5851	$5.9^{+0.94}_{-0.6}$	$4.6^{+1.8}_{-1.8}$	5.2 ± 0.6	−1.4	…
21	12:01:54.9207	−18:52:58.1868	$6.0^{+1.88}_{-0.7}$	$4.2^{+2.6}_{-2.2}$	5.0 ± 0.6	−1.8	…
22	12:01:55.2100	−18:52:44.5775	$5.85^{+0.65}_{-0.55}$	$4.8^{+1.51}_{-1.6}$	4.8 ± 0.5	−1.0	…
23	12:01:54.8877	−18:52:44.9757	$6.1^{+2.32}_{-0.7}$	$4.0^{+2.8}_{-2.2}$	4.5 ± 0.5	−0.9	…
24	12:01:54.5911	−18:52:43.9664	$5.95^{+1.93}_{-0.65}$	$4.4^{+2.8}_{-2.4}$	4.6 ± 0.5	−1.1	…
25	12:01:55.3198	−18:52:40.0113	$6.0^{+2.57}_{-0.67}$	$4.6^{+3.2}_{-2.5}$	4.7 ± 0.4	−1.1	…
26	12:01:55.0671	−18:52:39.5032	$5.8^{+0.5}_{-0.5}$	$4.6^{+1.2}_{-1.2}$	5.3 ± 0.6	−1.4	…
27	12:01:55.3381	−18:52:37.9582	$5.8^{+0.6}_{-0.5}$	$3.8^{+1.2}_{-1.2}$	4.4 ± 0.5	−0.8	…
28	12:01:55.1514	−18:52:37.9582	$5.9^{+1.12}_{-0.6}$	$4.2^{+1.4}_{-1.2}$	4.8 ± 0.5	−1.0	…
29	12:01:56.0486	−18:52:34.9713	$6.4^{+0.57}_{-0.8}$	$1.4^{+0.27}_{-0.41}$	4.9 ± 0.1	−1.5	…
30	12:01:54.7449	−18:52:31.3664	$5.7^{+0.5}_{-0.4}$	$5.4^{+1.2}_{-1.2}$	5.5 ± 0.8	−1.1	NU4A-6
31	12:01:54.9426	−18:52:29.2790	$5.7^{+0.5}_{-0.4}$	$3.8^{+0.4}_{-0.4}$	4.7 ± 0.6	−1.7	…
32	12:01:54.9646	−18:52:28.8464	$5.9^{+1.09}_{-0.6}$	$6.2^{+1.8}_{-1.6}$	4.8 ± 0.8	−1.4	…
33	12:01:54.5142	−18:52:28.7778	$5.7^{+0.6}_{-0.4}$	$3.2^{+0.8}_{-0.6}$	4.0 ± 0.6	−1.0	…
34	12:01:54.8547	−18:52:25.3171	$5.85^{+0.89}_{-0.55}$	$4.8^{+2.2}_{-1.8}$	4.8 ± 0.7	−1.3	…
35	12:01:54.5874	−18:51:56.5535	$6.4^{+0.74}_{-0.81}$	$2.8^{+0.63}_{-0.53}$	5.6 ± 0.3	−1.5	NU6-1
36	12:01:54.4995	−18:51:46.1852	$5.8^{+0.53}_{-0.5}$	$2.4^{+0.6}_{-0.6}$	4.5 ± 0.2	−0.8	…
37	12:01:55.1770	−18:51:41.0765	$6.4^{+0.41}_{-1.11}$	$3.2^{+0.58}_{-0.43}$	4.6 ± 0.9	−1.7	…
38	12:01:55.1624	−18:51:40.4311	$6.4^{+0.62}_{-1.05}$	$2.0^{+0.46}_{-0.62}$	4.5 ± 0.3	−1.3	…
39	12:01:53.1299	−18:51:38.2338	$6.2^{+0.56}_{-0.82}$	$3.4^{+0.84}_{-0.8}$	4.3 ± 0.5	−1.2	…
40	12:01:52.1558	−18:51:38.8106	$5.9^{+1.3}_{-0.6}$	$4.0^{+1.6}_{-1.4}$	4.8 ± 0.4	−1.4	…
41	12:01:52.0972	−18:51:40.3555	$5.9^{+1.17}_{-0.6}$	$4.4^{+1.8}_{-1.6}$	4.4 ± 0.3	−1.1	…
42	12:01:51.9690	−18:51:38.1239	$6.3^{+0.58}_{-0.81}$	$3.6^{+0.61}_{-0.56}$	5.3 ± 0.4	−1.4	…
43	12:01:51.0498	−18:51:58.2838	$5.7^{+0.5}_{-0.4}$	$4.0^{+0.4}_{-0.4}$	4.3 ± 0.4	−1.3	…
44	12:01:50.7971	−18:52:15.9993	$6.4^{+0.57}_{-0.81}$	$4.4^{+0.75}_{-0.96}$	5.0 ± 0.5	−1.6	…
45	12:01:50.9436	−18:52:28.0911	$6.2^{+0.67}_{-0.71}$	$3.0^{+0.83}_{-0.83}$	4.9 ± 0.3	−1.1	…

Notes. The last column cross-lists the ID for radio sources identified by S. G. Neff & J. S. Ulvestad (2000).
[a] The aperture correction listed for each cluster is the magnitude difference measured between aperture radii of 15 and 5 pixels, Δm_{5-15} pix, in the NIRCAM F360W filter.

(This table is available in its entirety in machine-readable form in the online article.)

using inverse variance weighting. After this normalization, we determine χ^2 values for each predicted combination of age and reddening:

$$\chi^2 = \sum_{i=1}^{N} \left(\frac{m_{\mathrm{model},\,i} - m_{\mathrm{obs},\,i}}{\sigma(m_{\mathrm{obs},\,i})} \right)^2, \quad (1)$$

where N is the number of filter passbands being fitted, and $\sigma(m_{\mathrm{obs},i})$ represents the observational uncertainty (in magnitudes) for the filter.

Uncertainties for log (age/yr) and A_V are determined as the values within ±34 percentile of the lowest χ^{-2} value, equivalent to $\pm 1\sigma$ for a normal distribution. The log (age/yr)

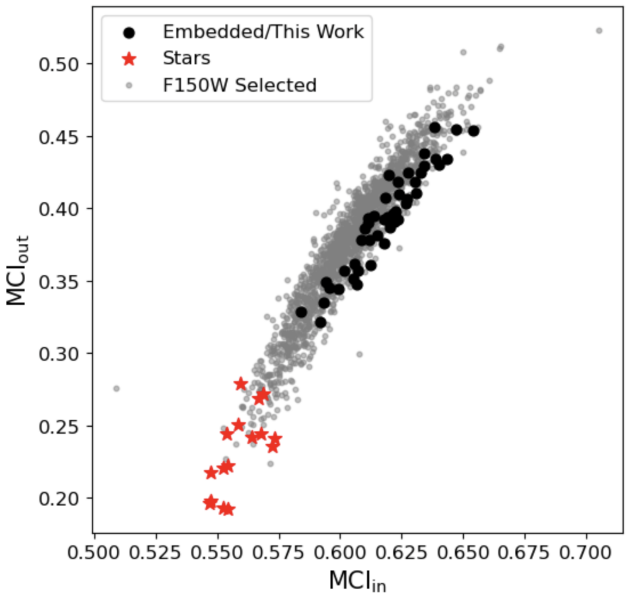

Figure 5. Structural properties measured in the F360W filter for the embedded cluster candidates detected in this work (black circles) are compared with a training set of stars (red symbols) and a new catalog of F150W-selected clusters (gray points). The embedded sources overlap with the cluster sample. MCI measures the magnitude differences between different apertures and is a simple method to determine object size. The definitions of MCI_{in} and MCI_{out} are given in Section 3.1.

versus A_V grid is oversampled by a factor of 10 in this step, using linear interpolation. The mass and associated uncertainty are calculated from the extinction-corrected F360W magnitude and best fit, plus uncertainties for log (age) and A_V. The best-fit age, A_V, mass, and associated uncertainties are listed for each cluster in Columns (4)–(6) of Table 2.

4.2. Age, Extinction, Mass Results

In Figure 7, we show results from the SED fitting described above for 12 clusters from our sample. We show the photometry measured in all 11 HST+JWST filters (data points) and the best-fit results (solid line) based on the procedure described above. Photometric uncertainties are included, but are mostly smaller than the data points. The panels show examples of similar-age clusters with high A_V ($\approx$6−7 mag, top panel), moderate A_V ($\approx$4 mag, middle panel), and low A_V ($\approx$2.5 mag, bottom panel) from our sample.

Overall, the fits look quite good. As expected, all clusters in the sample are very young with a best-fit age of $\approx$2.5 Myr or younger, and the shape of the SED is mainly driven by extinction. We see that none of the Antennae clusters with the highest extinction (including WS80) are detected in the F275W/NUV or F336W/U filters, and that their measured and best-fit continuum slopes drop sharply toward short (blue) wavelengths. Despite experiencing high extinction, Hα emission is detected from massive clusters with $A_V \gtrsim 6$ mag. Clusters with moderate extinction have shallower slopes (decrease less) toward short wavelengths and have strong emission lines, and those with low extinction have SEDs that are flat or increase toward the NUV.

In Figure 8 (central panel), we plot the best-fit mass versus A_V for each embedded cluster in our sample. The clusters have a range of extinction A_V between $\approx$2 and 10 mag. The histogram along the right side shows a predominant value of

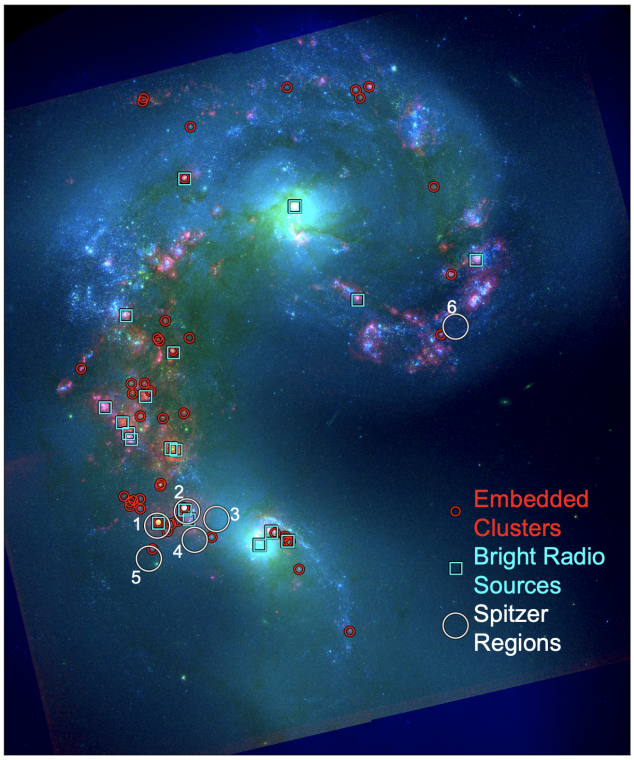

Figure 6. Locations of the embedded clusters identified in this work are shown by the red circles. All 19 "bright" radio sources (6 cm flux $\gtrsim$200 mJy; see Appendix) are shown as cyan squares, and the six apertures (circles with a 2.″55 radius) used to extract Spitzer/IRS spectra are shown as the white circles. The background color image is a combination of V-F150W-Paα filters.

$A_V \approx 4$ mag. The embedded clusters have estimated masses (listed in Column (6) of Table 2) that range from $\approx 3 \times 10^4\, M_\odot$ to $\approx 3 \times 10^6\, M_\odot$. Overall, we see there are fewer high-mass clusters (the distribution of embedded cluster masses will be discussed in Section 5.3) and fewer clusters with high extinction.

4.3. Comparison with Published Cluster Properties

Our estimates of the age, extinction, and mass for the most massive embedded cluster in the Antennae, WS80, agree well with many previously published results. We find this cluster has an age log $(\tau/\mathrm{yr}) = 6.3^{+0.63}_{-0.80}$, $A_V = 9.2^{+1.36}_{-1.16}$ mag (the highest in our sample), and an estimated mass of at least log $(M/M_\odot) = 6.5$ (for this cluster and its neighbor, the aperture corrections are lower limits). Our age compares well with published estimates of log $(\tau/\mathrm{yr}) \approx 6.0$ (e.g., B. C. Whitmore et al. 2010). Published values of extinction include $A_V = 7.3$ mag (B. C. Whitmore et al. 2010) and $\approx$9−10 mag (A. M. Gilbert et al. 2000), and the published range of masses is between 10^6 and $10^7\, M_\odot$ (B. C. Whitmore & F. Schweizer 1995; A. M. Gilbert & J. R. Graham 2007; B. C. Whitmore et al. 2010; C. N. Herrera & F. Boulanger 2017).

The companion to WS80 is also quite young with a best-fit age of log $(\tau/\mathrm{yr}) = 6.4$, $A_V = 3.4 \pm 0.2$ mag, and log $(M/M_\odot) = 5.9$. Previously, B. C. Whitmore et al. (2010) estimated log $(\tau/\mathrm{yr}) = 6.4$, $A_V \approx 3$ mag, and log $(M/M_\odot) = 6.6$ from optical photometry alone. Our embedded cluster #30 has best-fit values of log $(\tau/\mathrm{yr}) < 6.0$, $A_V = 5.4 \pm 1.2$ mag, and log $(M/M_\odot) = 5.5$, in good agreement with the

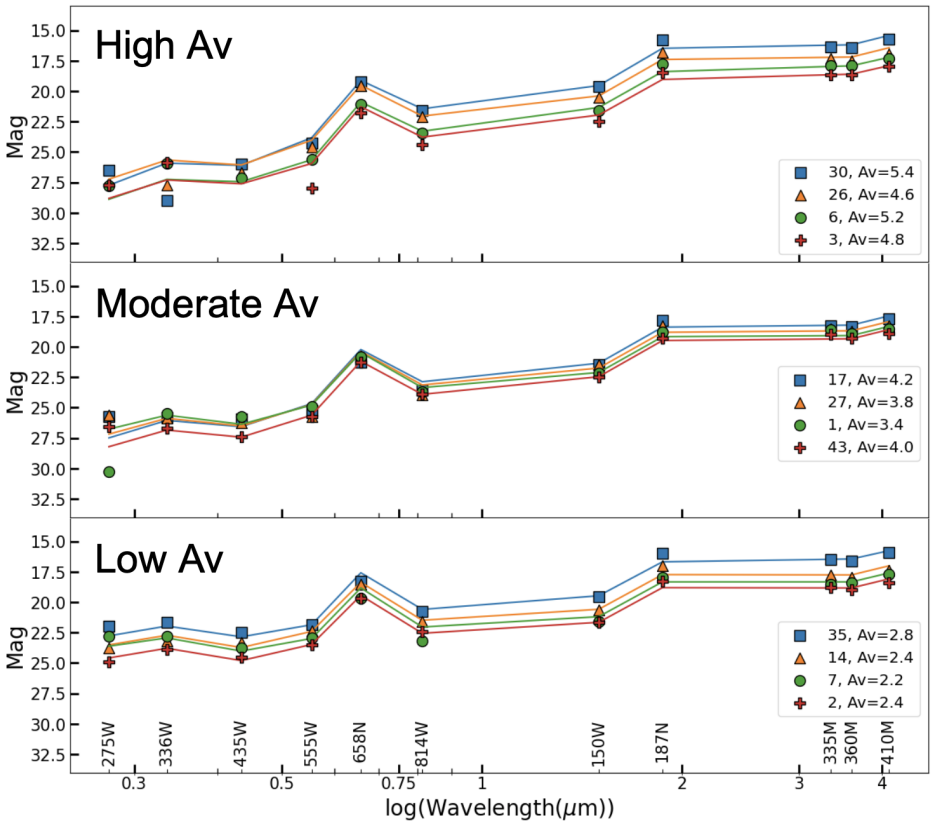

Figure 7. Observed photometry and best-fit SEDs for a subset of clusters with high (top), moderate (middle), and low (bottom) extinction A_V. Photometric uncertainties are included, but are mostly smaller than the symbol size. All of the embedded clusters are very young, with best-fit ages $\lesssim$2.5 Myr, so their SEDs are driven mostly by extinction. Differences in the shapes of the SED can be seen, with the high-A_V clusters becoming quite faint at short wavelengths (many are not detected in the NUV and U filters), the low-A_V clusters have blue SEDs, while those with moderate A_V have intermediate slopes at short wavelengths. Note that Hα emission is detected in most embedded clusters, even those with the highest A_V.

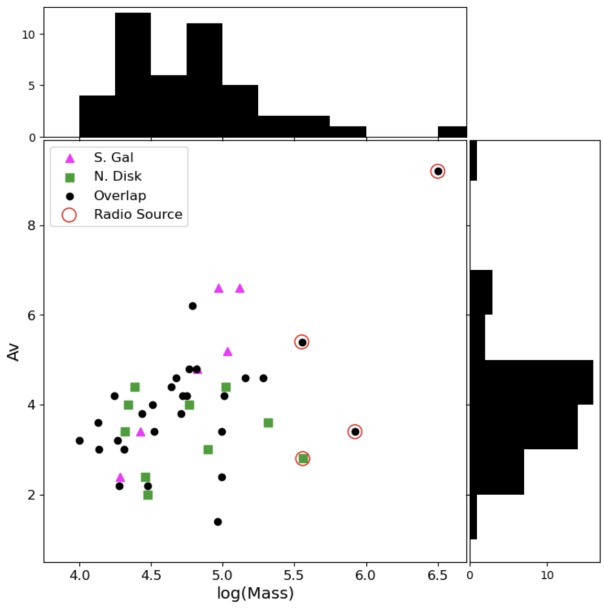

Figure 8. Best-fit mass and extinction A_V for the embedded cluster sample. Clusters in the southern galaxy are plotted in purple, the overlap region in black, and the northern disk in green. All clusters have estimated ages of 2.5 Myr or younger. The A_V values range from $\approx$2 mag up to $\approx$10 mag, with half the sample (22 of 45) having a best-fit A_V of 4 mag or higher. The red circles show that clusters also detected at radio wavelengths are the most massive in our sample (see Section 5.4).

B. C. Whitmore et al. (2010) results of log (τ/yr) $\approx$ 6.0, $A_V \approx 4$ mag, and log ($M/M_\odot$) $\approx$ 6.0.

H. He et al. (2022) estimated the optical extinction A_V toward several clusters, including WS80 and its neighbor, from high-resolution continuum observations at 100 and 345 GHz taken with ALMA. They derived extinction values from estimates of the gas surface density, and found $A_V \approx 2200$ mag and $\approx$450 mag for WS80 and its neighbor, respectively, significantly higher than the estimates presented here, although their calculations rely on assuming the shape of the thermal dust and free–free spectral indices. It is possible that the frequency coverage of their radio observations is insufficient to constrain cluster extinction.

5. Discussion

5.1. Nowhere Left to Hide

Some of the most intense star formation in the nearby Universe is happening in merging galaxies. Since star formation takes place in dense, dusty molecular clouds, the earliest stages of star and cluster formation are obscured at optical wavelengths. However it still is not known whether most sites of cluster formation are optically obscured and embedded in thick layers of dust with $A_V \approx 40-70$ mag (e.g., S. A. Stanford et al. 1990; D. Kunze et al. 1996; I. F. Mirabel et al. 1998; U. Klaas et al. 2010), or if most (massive) clusters have $A_V \lesssim 10$ mag and have already been detected at optical wavelengths (B. C. Whitmore & Q. Zhang 2002). With our

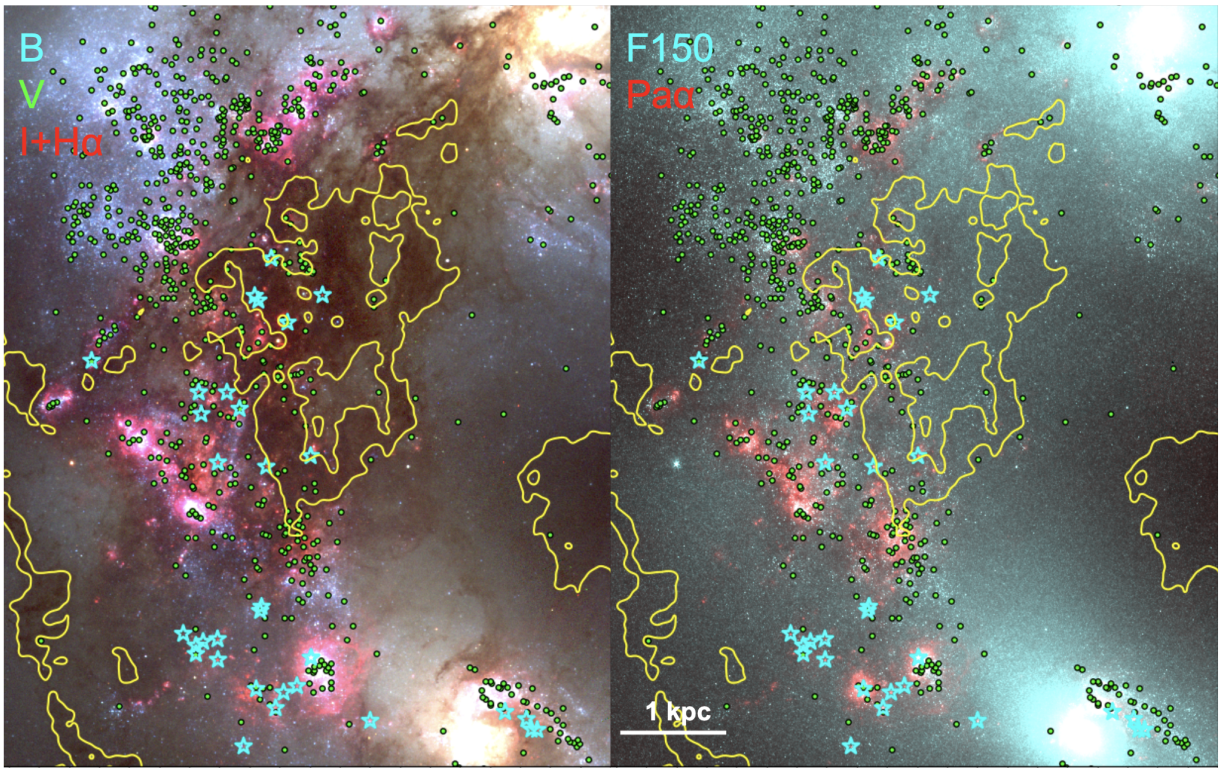

Figure 9. Few clusters (of any age) are forming in the prominent, dark dusty regions seen in optical images of the overlap region in the Antennae. This indicates the ISM in these regions is not currently participating in star formation and is likely in the foreground. Different combinations of optical and infrared filters are shown in each panel (as indicated). Contours identify dark regions in the *B*-band image, small green circles show the locations of the F150W-detected clusters, and the cyan stars show the locations and amount of ionization from very young clusters.

deep, high-resolution infrared JWST images, we are now in a position to directly answer this question by uncovering the deeply embedded, recently formed cluster population in the Antennae.

We believe there are no massive clusters with $A_V \gtrsim 10$ mag in the Antennae, and that we have uncovered essentially all clusters with $M \gtrsim 3 \times 10^4\,M_\odot$ and extinction $A_V \gtrsim 2$ mag. One key clue is that we did not find any sources that have Brα but no Paα emission; Paα emission generally indicates that a source must have extinction A_V less than 20 mag. More quantitatively, we can estimate the range of detectable A_V for a given mass by scaling the observed parameters of WS80, which has a mass $M \approx 3 \times 10^6\,M_\odot$, extinction $A_V \approx 10$ mag, and is ≈7 mag brighter than the detection limit in the Paα filter. Since $A_{\rm Pa\alpha} \approx 0.1 \times A_V$, if WS80 experienced no extinction, it would be ≈8 mag brighter than the detection limit. Simple scaling arguments indicate that our Paα observations are sufficiently deep to detect $3 \times 10^5\,M_\odot$ ($3 \times 10^4\,M_\odot$) clusters with extinction A_V up to ≈55 mag (≈30 mag). All but 13 of the embedded clusters have masses $M \gtrsim 3 \times 10^4\,M_\odot$, so the Antennae have formed plenty of massive clusters; we just do not detect any with extinction higher than $A_V \approx 10$ mag.

We estimate the fraction of very young clusters missing from optical surveys by combining our new embedded cluster list with the HST-based cluster catalog published by B. C. Whitmore et al. (2010). We adopt a mass limit of $3 \times 10^4\,M_\odot$, the approximate completeness limit for the embedded cluster catalog (see Section 5.3). Our new catalog has 38 clusters above this mass limit, but four are included in the optical catalog, so there are 34 unique new clusters above the completeness limit. The B. C. Whitmore et al. (2010) catalog has 156 clusters younger than $\tau \leqslant 3$ Myr and more massive than $3 \times 10^4\,M_\odot$, suggesting their optical study is missing ≈18% (34/(156 + 34)) by number of these very young clusters in the Antennae. If we consider the 306 (788) optically selected clusters above this mass that have estimated ages ⩽10 Myr (⩽100 Myr), this percentage drops to ≈10% (≈4%), which represents a small fraction of the total *number* of clusters in the Antennae. While the embedded population is just a few percent of the total cluster population, it emits the majority (≈60%) of the total ionizing photon luminosity in the Antennae, with WS80 alone emitting ≈27% of the ionizing photons based on estimates from the ages and masses of the embedded and optically detected clusters. This is consistent with the 15% of the total 12.5–18 μm luminosity measured for WS80 (I. F. Mirabel et al. 1998).

Figure 9 illustrates that star formation, traced in pink by Hα (left) and Paα (right), is ongoing throughout much of the overlap region, with no obvious pattern from east to west. However, little star formation is taking place in a number of optically dark, dusty regions. The yellow contours highlight dark regions in the *B*-band image. It is clear that there are very few embedded clusters forming in these dusty regions (cyan stars), or clusters of any age, since there are almost no small green circles (candidate star clusters selected in the JWST/F150W image) within the contours. The most likely explanation for the dust lanes and clusters having different spatial distributions is that the dust is cold and in the foreground of any optically emitting material. In fact, the brightest clusters in our Brα and 3.6 μm infrared images do not coincide with the most prominent dark, dust-affected areas in the optical HST

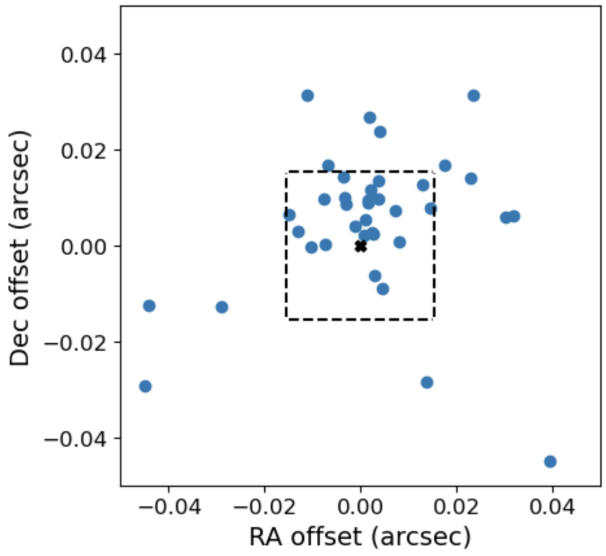

Figure 10. Offsets (in arcseconds) between the measured centers of the embedded clusters in the F187N (Paα) and F150W (stellar continuum) filters, where 1″ subtends 104 pc at the distance of the Antennae. The dashed box shows the size of an NIRCAM short-wavelength pixel. Despite Paα and 1.5 μm originating from different processes, we see that the sources peak in similar locations in both filters. Some of the embedded clusters are quite faint at 1.5 μm, while others are somewhat extended in Paα, which likely contributes some scatter to the measurements. Overall, the emission from recombination lines and stellar continuum is consistent with zero spatial offset for these very young, embedded clusters.

images, indicating that much of the dust/ISM in the overlap region is not hiding any significant amount of star formation.

5.2. The Embedded Cluster Population in the Antennae

Massive stars formed in very young $\lesssim$3 Myr clusters ionize the gas in their immediate vicinity, but live inside a larger, surrounding cloud of neutral and molecular gas. Presupernova stellar feedback (stellar winds, photoionization, and radiation pressure) can carve channels in the ISM through which the starlight and ionizing radiation can escape (e.g., D. G. Whelan et al. 2011; C. Howard et al. 2017), although the timescale for this process is not well constrained.

We assess the multiwavelength contributions of ionized gas, stellar continuum, and dust emission from the embedded clusters based on the JWST+HST images and their measured photometry. All embedded clusters have compact Paα and Brα emission, but nine of them (#2, 3, 4, 7, 10, 24, 31, 36, 37) have no detectable or very weak Hα emission. All have detected stellar continuum emission at 1.5 μm, and all have strong 3.6 μm emission. We also detect compact 3.3 μm PAH emission from all of the embedded clusters except for #4, which is the closest source to the southern nucleus and has a strange SED; 3.3 μm PAH emission has been shown to decrease toward the nucleus of at least one nearby Seyfert galaxy (NGC 7469; T. S. Y. Lai et al. 2023).

H. He et al. (2022) suggested that the near-infrared and radio emission from embedded clusters might originate from slightly different parts of the dense molecular cloud, as predicted by the "blister" model, as a possible explanation for the high extinction values they derived (Section 4.3). In Figure 10, we present the spatial offsets in arcseconds measured between Paα (ionized gas) and 1.5 μm (stellar continuum) emission, where each cluster was centered individually in each image. The dashed square represents the size of an NIRCAM pixel. The figure shows that the stellar continuum and ionized gas emission peak at similar locations, as expected for massive clusters with $A_V \lesssim 10$ mag. Quantitatively, we find that the embedded cluster locations in Paα and 1.5 μm are consistent with zero mean offset, with ΔR.A. $= -0\farcs01 \pm 0\farcs09$, and Δdecl. $= 0\farcs01 \pm 0\farcs03$. All of the embedded clusters in our new catalog have estimated ages of 2.5 Myr and younger, with the majority being dated to ages of just 1 Myr or less. The fact that we detect starlight (even if faint) at 1.5 μm from the embedded clusters from these very young clusters indicates that presupernova feedback carves channels in the dense ISM within $\approx$1 Myr, allowing recombination line emission and starlight to escape the parent molecular cloud (e.g., J. Kim et al. 2021; L. Ramambason et al. 2026), and essentially rules out the blister model for the sources studied here. It is not just the most massive clusters that have such short emergence timescales. Starlight (1.5 μm emission) is detected from clusters over the full observed mass range, suggesting this timescale does not have a strong dependence on cluster mass in the Antennae.

We checked for differences in cluster properties based on location within the Antennae, considering clusters in the south galaxy (mostly near the nucleus, sources #1–6), the overlap region between the two galaxies (#7–34), and the north galaxy disk (#35–45). The estimated mass versus A_V for clusters in the three locations is shown in Figure 8. Clusters with masses higher than a few $\times 10^4\,M_\odot$ are forming throughout the Antennae, but the most massive clusters only form in the overlap region. Clusters with the highest extinction ($A_V \gtrsim 5$ mag) are in the overlap region (black circles) and in the star-forming arc around the southern nucleus (purple triangles), while embedded clusters in the disk of the north galaxy (green squares) have systematically lower extinction, all with $A_V \lesssim 4$ mag. There is no obvious variation in the age estimates with location.

5.3. Embedded (Initial) Cluster Mass Function

The recent formation of massive clusters in the Antennae makes it an ideal system to assess the shape of the initial cluster mass function. The cumulative mass distribution of the embedded clusters in the Antennae clearly extends above $10^6\,M_\odot$, as shown in Figure 11 (left panel). A lower mass limit of $\log(M/M_\odot) = 4.2$ (dashed vertical line) is determined from the deviation (flattening) of the distribution from a power law. A power law, $dN/dM \propto M^\beta$, is a good representation of the data, and we find a best-fit value of $\beta = -1.8 \pm 0.1$, shown by the dashed–dotted line in the figure. This result is similar to the power-law index of $\beta \approx -2$ found for the mass function of young clusters in many other nearby star-forming galaxies (e.g., Q. Zhang & S. M. Fall 1999; A. Bik et al. 2003; N. McCrady & J. R. Graham 2007). While a parsec-scale simulation of an Antennae-like system suggests that the mass function of the gas flattens in regions of very high pressure (H. Li et al. 2020), we do not find strong evidence for this. It is worth noting that nearly all previous works include clusters with ages between 1 and 10 Myr in their fits, which may already have experienced some evolution, whereas our distribution includes only the very youngest ($\lesssim$2.5 Myr) clusters and is therefore a better representation of the "initial" cluster mass function.

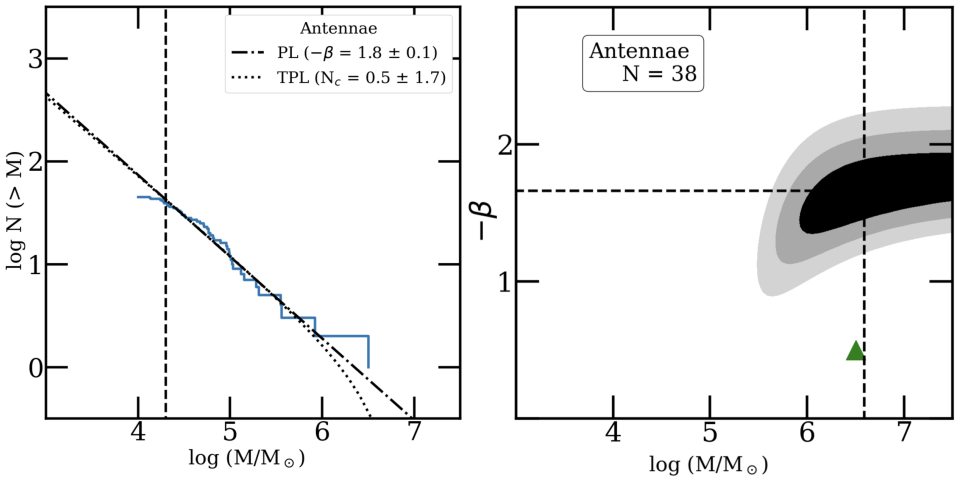

Figure 11. Left: cumulative mass function of the embedded cluster sample. The completeness limit is shown as the dashed vertical line and determined to be at the mass where the distribution flattens from a power law. The best power-law fit is shown as the dotted–dashed line, and has an index of $\beta = -1.8 \pm 0.1$. The best truncated power-law fit is shown as the dotted line, and the statistic N_C, which gives the number of embedded clusters above the truncation mass, is not statistically significant, suggesting that no truncation mass is detected at the upper end of the distribution. Right: The contours show 1σ (black), 2σ (gray), and 3σ (light gray) confidence intervals for the power-law index $-\beta$ and upper mass cutoff M_* for the maximum likelihood fit to a Schechter function for the embedded clusters above the mass limit. The most massive cluster is plotted as the green triangle. The upper mass cutoff M_* does not converge for the embedded cluster sample presented here, indicating there is no preference for a Schechter-like cutoff over a power law.

To assess whether the high-mass end of the embedded cluster distribution shows any hint of a downturn or cutoff, we first fit a truncated power law to the cumulative distribution using the MSPECFIT software (E. Rosolowsky 2005). The results are shown by the dotted line in the left panel of Figure 11. The N_C value of 0.5 ± 1.7, the number of embedded clusters above the truncation mass, indicates there is no statistically significant truncation found in the distribution. Because binned distributions can hide weak features at the ends of the distribution, we also fit a Schechter function, $dN/dM \propto M^{\beta} \exp(-M/M_*)$ with power-law index β and exponential cutoff M_*, using the maximum likelihood method developed in A. Mok et al. (2019). The resulting 1σ, 2σ, and 3σ contours for β and M_* are shown in the right panel of Figure 11. The green triangle indicates the most massive embedded cluster in the sample, and the dashed lines show the best formal fit to β and M_*. However, all of the contours remain open to the highest mass allowed in the fit, indicating this value of cutoff mass M_* is essentially a lower limit. This preliminary result suggests that the initial cluster mass function continues as a power law to masses above $10^6\,M_\odot$ in galaxies with intense star formation, and that the exponential-like downturn observed in the high end of the GC mass function may result from evolution rather than be imprinted during formation (S. M. Fall & Q. Zhang 2001).

5.4. No Infrared-dark Thermal Radio Sources in the Antennae

Radio observations are considered the gold standard for identifying deeply embedded star clusters, since they detect thermal free–free continuum emission from gas ionized by recently formed massive stars (H. A. Kobulnicky & K. E. Johnson 1999; K. E. Johnson et al. 2001, 2004, 2009; K. E. Johnson & H. A. Kobulnicky 2003; A. G. Aversa et al. 2011; A. A. Kepley et al. 2014) and are unaffected by high extinction caused by large amounts of dust (E. J. Murphy et al. 2011). In the Appendix, we identify the infrared counterparts to 6 cm sources cataloged by S. G. Neff & J. S. Ulvestad (2000) and a subset of seven sources identified by H. He et al. (2022) at 100, 200, and 345 GHz, and summarize the results of that investigation here.

We identify four and possibly five of the radio sources as embedded clusters from their high Paα/Hα and Brα/Hα flux ratios. These include WS80 (#9), its neighbor (#13), and two other sources in the overlap region (#30, #35). One near the southern nucleus (#4) may also have radio emission. These sources have a range of extinction, with three having among the highest in our sample, with $A_V \gtrsim 6$ mag, and two with more moderate values of $A_V \approx 3$ mag. The clusters associated with these radio sources are the most massive in our sample (red circles in Figure 8), with $M \gtrsim$ few $\times\, 10^5\,M_\odot$. Two of the sources (4–4 and 8–4 from S. G. Neff & J. S. Ulvestad 2000) have bright Paα, optical, and near-infrared emission with low Paα/Hα and Brα/Hα flux ratios, and appear to be optically bright star clusters with low extinction. We did not find any published radio properties (e.g., spectral index or flux ratios) that appear to correlate with extinction, although there are only a few clusters, and the published radio properties are incomplete. The remaining 10 nonnuclear radio sources listed in the Appendix do not appear to be associated with clusters at all and may be nonthermal (e.g., supernova remnants). Some of these show a bubble-like Paα morphology with no obvious counterpart in the broadband JWST images, and include two sources in the Firecracker region (3-5A and 3-5B).

We find no thermal radio sources that are infrared-dark, since all are detected in the 1.5 μm through 4.05 μm JWST images. The thermal radio sources are detected in all of our infrared filters, but 40 of the 45 embedded clusters discovered here have no radio counterpart. These "radio-dark" clusters mostly have estimated masses less than $\lesssim 10^5\,M_\odot$. Thermal radio sources in the Antennae include deeply embedded clusters (A_V up to $\approx$10 mag), but also clusters that are optically bright and experiencing little extinction. Regardless of the amount of extinction, only the most massive clusters ($M \gtrsim$ few $\times\, 10^5\,M_\odot$) are identified in current radio surveys of the Antennae.

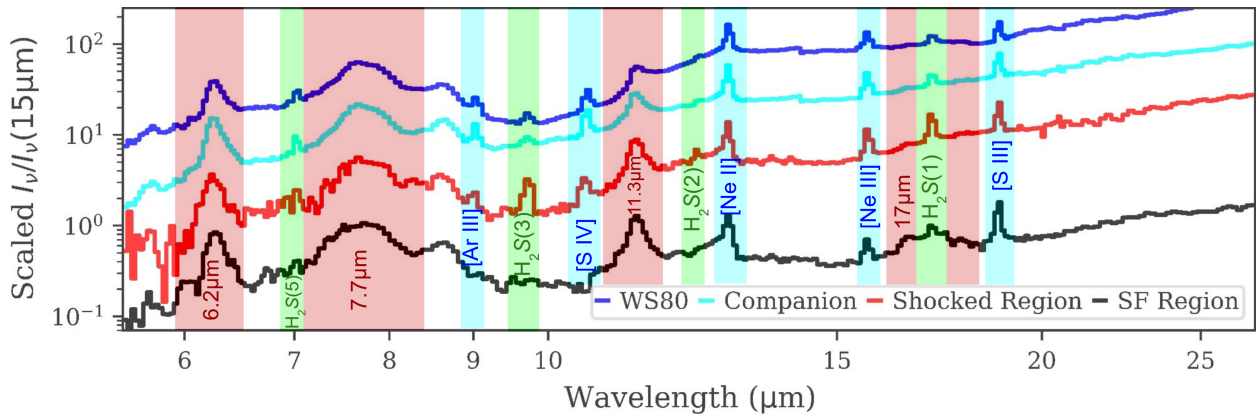

Figure 12. Extracted Spitzer/IRS spectra of WS80 (dark blue), its companion (cyan), a region of shock-heated ISM just below the cluster pair (red, designated region 3 in Figure 6), and a random star-forming region in the north disk. Key diagnostic features are highlighted, including the main PAH bands, low- and high-ionization metal, H_2 rotational, and H recombination lines. Note the strong H_2 lines in the shock-heated region.

The estimated depth of the two radio surveys discussed above is consistent with the cluster mass limits we have found here. In particular, H. He et al. (2022) find that 100 GHz continuum point sources detected with ALMA at a signal-to-noise ratio $\geqslant 5$ correspond to star clusters with a derived stellar mass of several $\times 10^5\,M_\odot$. Given the much lower number of 100 GHz detections (17) compared with expectations from existing optically surveys ($\sim$200), H. He et al. (2022) conclude that they detect so few embedded clusters because of their high-mass limit, plus the short-lived phase when embedded clusters are bright at submillimeter wavelengths. The S. G. Neff & J. S. Ulvestad (2000) radio survey has a 5σ point-source detection limit of 50 μJy at 4 and 6 cm, which corresponds to a luminosity of $\sim 3 \times 10^{25}$ erg s^{-1} Hz^{-1}. We calculate an ionizing photon rate of $\approx 10^{51}$ from this luminosity using Equation (10) in E. J. Murphy et al. (2011; for an assumed thermal fraction of 50% at 5 GHz), which is expected from very young clusters with masses $\approx 10^5\,M_\odot$ (K. L. Emig et al. 2020). Free–free absorption could potentially suppress the 6 cm thermal flux from embedded clusters, which would effectively raise this mass threshold further. Our infrared line-ratio-based selection method, therefore, detects embedded clusters that are $\approx 10\times$ less massive than current radio surveys in the Antennae.

5.5. Constraints on the Formation of Very Massive Clusters

Now that we have identified all of the obscured clusters more massive than a few $\times 10^4\,M_\odot$, we are confident that WS80 and its companion, both with masses $\gtrsim 10^6\,M_\odot$, are the two most massive recently formed clusters in the Antennae. This massive cluster pair has formed in a special location, at the edge of a supergiant molecular cloud, very close to the southern edge where the two galaxies overlap, which may offer clues to the specific processes responsible for their formation.

Diffuse, soft X-ray emission is observed just to the south of the clusters in Chandra X-ray Observatory images (G. Fabbiano et al. 2001), suggesting there is shock-heated gas nearby. However, previous infrared-based studies have reached different conclusions about the presence of shocked gas. M. Haas et al. (2005) concluded that strong H_2 S(3) emission observed in an Infrared Space Observatory spectrum covering most of the Antennae (including the overlap region and both nuclei) likely originated from large-scale shocks due to the collision between H I clouds. Conversely, B. R. Brandl et al. (2012) found from Spitzer spectra that the H_2 emission in the overlap region agrees well with active star formation and that far-ultraviolet photons and local shocks from supernovae are likely responsible for exciting the molecular hydrogen rather than shocks from the large-scale interaction of the two galaxies. They did not, however, specifically extract spectra from regions surrounding WS80 and its companion.

Here, we revisit the H_2 emission near this remarkable pair of massive star clusters. We use SIMLA cubes (see G. P. Donnelly et al. 2025, Section 2.4) to extract Spitzer spectra for WS80, its companion, three regions just south of the massive cluster pair (overlapping the diffuse X-ray emission), and a control region in the northern disk using a 2.″5 aperture radius ($\sim$smallest reasonable aperture for the observations), although the main results are not sensitive to the exact aperture size or location. Extracted spectra are shown in Figure 12, and their apertures are indicated as the larger white circles in Figure 6. Key diagnostic features in the spectra are highlighted in Figure 12, including the main PAH bands (pink), low- and high-ionization metal lines (light blue), and H_2 rotational lines (light green). The PAH bands at 6.2, 7.7, and 11.3 μm are strong in the spectrum of both WS80 and its companion cluster, and WS80 in particular shows a significant amount of absorption. Figure 12 also shows a spectrum (in red) of region 3, located south of the clusters. PAH features and nebular emission lines are observed in the spectrum. One key difference, however, is that the H_2 lines in region 3 are clearly stronger than those associated with the clusters themselves. In an upcoming work, we will present a detailed analysis of the Spitzer spectra for $\approx$20 of the brightest young clusters throughout the Antennae and tens of regions between them.

Observations and radiation modeling have shown that the H_2/PAH ratio can be used as a diagnostic to identify regions heated primarily by star formation and those with additional heating from shocked gas (e.g., P. Ogle et al. 2010; P. Guillard et al. 2012). PAH molecules are excited primarily by UV photons, but H_2 molecules will experience additional heating if shocks are present, so the ratio of H_2 to PAH emission is higher in regions with additional mechanical heating than in normal star-forming regions. We measure the strengths of the 7.7 μm PAH feature and the four H_2 S(0), S(1), S(2), and S(3) lines, which are summed together to produce H_2 S(0–3). The strength of these features is determined from PAHFIT, which

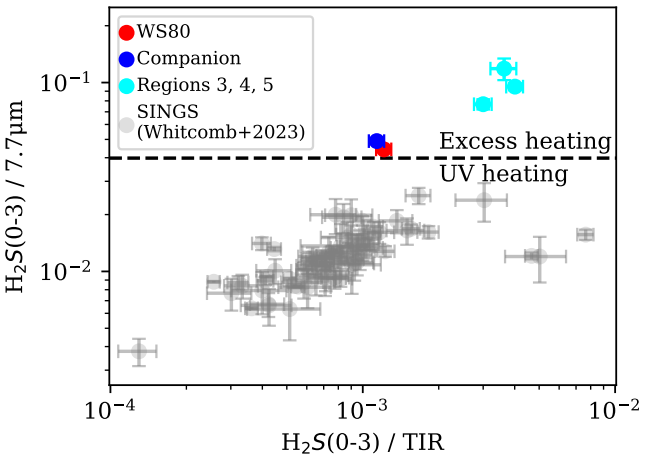

Figure 13. The measured ratios of the (summed) H_2 S(0–3) lines to 7.7 μm PAH feature are plotted for the massive embedded cluster pair WS80 and its companion, a random star-forming (SF) region in the north disk, and three regions of ISM just south of the clusters (their locations are shown in Figure 6). The dashed horizontal line shows the typical value measured for H_2/PAH in photodissociation regions associated with star formation. The ISM regions have significantly stronger ratios, indicating they are affected by excess heating, likely from shocks.

models the mid-infrared spectrum as a combination of blackbodies of fixed temperature, Gaussian emission lines, Drude profiles for PAH subfeature emission, and a power law describing silicate extinction with features at 9.7 and 18 μm. PAHFIT is also used to combine subfeatures and propagate uncertainties to derive the intensity of the 7.7 μm complex (see J. D. T. Smith et al. 2007 for more details).

The ratio measured for the six extracted regions is plotted in Figure 13. The dashed line at 0.04 represents the near-constant ratio between the H_2 S(0–3) line and the 7.7 μm PAH feature determined for normal star-forming regions with a large range of infrared luminosities (P. Ogle et al. 2010). The star-forming region in the northern disk and the companion to WS80 both have measured H_2/PAH ratios that are consistent with $\sim$0.04. Meanwhile, the three regions just below the massive cluster pair (designated 3, 4, 5) have significantly higher H_2/PAH ratios, $\approx$0.10$-$0.12. These regions are unlikely to be excited by an AGN in the nucleus of NGC 4039, since the ratio is strongest for region 6, which is the furthest away. The H_2/PAH ratio for WS80 is somewhat higher than that found for normal star-forming regions in nearby galaxies as part of the SINGS sample (gray points; C. M. Whitcomb et al. 2023), but it is possible that some shocked-heated gas is included in the aperture. These results support a picture where shocks are responsible for the elevated H_2/PAH ratios measured in areas just surrounding WS80 and its companion. Higher spatial resolution observations would help map out the strength and spatial distribution of the shocks in this region.

All of the clues discussed in this section for the massive cluster pair are consistent with the picture of massive cluster formation in merging galaxies suggested by C. J. Jog & P. M. Solomon (1992). In their analytical models, they separately followed atomic and molecular hydrogen during a merger between two galaxies, and found that typically H I clouds collide, but molecular clouds, which have smaller volume filling factors, do not. The collisions between H I clouds result in radiative shock compression of the outer layers of nearby, preexisting GMCs that then trigger the formation of massive clusters. Similarly, the fully hydrodynamic simulations of galaxy mergers performed by M. Maji et al. (2017) found that massive star clusters (with masses $\sim 3 \times 10^5 - 3 \times 10^7\,M_\odot$) preferentially form in the highly shocked regions found in galaxy interactions. Consistent with these predictions, WS80 and its companion cluster have formed near the southern edge of a supergiant molecular cloud (WS80 is still embedded in weak CO emission while its companion is not; H. He et al. 2022), which is adjacent to the shocked gas identified in regions 3, 4, and 5 studied here.

6. Summary and Conclusions

In this work, we presented new images of the merging Antennae galaxies taken with JWST in the F150W, F187N (Paα), F335M (3.3 μm PAH), F360M, and F410M (Brα) NIRCam filters and the F770W (7.7 μm PAH) MIRI filter. These observations, particularly when combined with archival images taken with HST in the F275W (NUV), F336W (U), F435W (B), F555W (V), F658N (Hα), and F814W (I) filters, give a new view of the star clusters and ISM in this iconic merging system. The JWST images penetrate even the dustiest portions of the overlap region, allowing us to identify and study the most recently formed and deeply embedded star clusters.

We discovered a population of 45 embedded cluster candidates in the Antennae with high Brα/Hα and/or Paα/Hα flux ratios, which are broader than the PSF at 3.6 μm. We did not identify any sources with Brα but no Paα emission; if such a source was detected, it would have extremely high extinction in the V band ($A_V > 20$ mag). The embedded clusters are detected at all wavelengths between 1.5 and 7.7 μm. Most of the embedded cluster population (28/45 or $\approx$60%) is located in the region where the two galaxies overlap, and most current star formation is taking place, with 11/45 or $\approx$25% forming in the northern disk and 6/45 or $\approx$15% near the southern nucleus.

We estimated the age, V-band extinction, and mass of each embedded cluster by fitting its measured 0.275–4.1 μm SEDs with predictions from the FSPS models of C. Conroy et al. (2009). These models include dust extinction and emission, nebular continuum, and line emission and fit the observed SEDs well. All embedded clusters have best-fit ages of 2.5 Myr and younger, with nearly 80% having best-fit ages consistent with 1 Myr or less. Estimates of extinction A_V range between $\approx$2 and 10 mag, and mass between $\approx 3 \times 10^4$ and $3 \times 10^6\,M_\odot$. The embedded cluster mass function can be described by a single power law with a formal best-fit index of $\beta = -1.7 \pm 0.1$, and shows no evidence for a downturn at the high-mass end.

The observations are sufficiently deep that we believe we have detected all clusters in the Antennae galaxies more massive than $3 \times 10^4\,M_\odot$ with $A_V \gtrsim 2$ mag. Previous suggestions that clusters deeply embedded in dusty cocoons with $A_V > 30$ mag dominate the infrared emission from the Antennae likely resulted from poorer resolution observations.

We compared the locations of the embedded clusters with those of thermal radio sources identified by S. G. Neff & J. S. Ulvestad (2000) and H. He et al. (2022), and with optically selected clusters in the B. C. Whitmore et al. (2010) catalog. The spatial analysis reveals:

1. Four and possibly five of the embedded clusters in our catalog are also thermal radio sources (#8, 12, 29, 34,

and possibly #3), including the well-known massive cluster pair WS80 (#8), which is highly embedded, and its nearby, more moderately extinguished massive companion cluster (#12). The remaining 40 sources are newly identified star clusters.

2. Three thermal radio sources (companion to WS80 plus 4-2A and 8-4 from S. G. Neff & J. S. Ulvestad 2000) are bright at optical wavelengths and included in the optically selected HST-based cluster catalog of B. C. Whitmore et al. (2010).
3. We were unable to identify a cluster associated with three other potential thermal radio sources in the JWST or HST images. There is Paα emission from these sources, but it has a different morphology than from the embedded clusters, with shells rather than a compact structure. These radio sources may be supernova remnants.
4. None of the currently known bright thermal radio sources are infrared-dark, and all are detected from 1.5 through 4.1 μm, suggesting they have moderate extinction.
5. Based on the derived properties, we found that current radio observations identify only the most massive clusters, including ones that are optically bright and have low extinction. It appears challenging to isolate the embedded phase of cluster evolution with only radio measurements.
6. When added to optically selected catalogs, the embedded sources provide a complete census of obscured and unobscured clusters. We estimated that optical studies are missing $\approx$15% of very young ($\lesssim$3 Myr) clusters in the Antennae. The newly discovered embedded cluster population is important for studying the earliest phases of cluster evolution, but represents a very small fraction ($\lesssim$3%) of the observable cluster population in the Antennae galaxies.

We found that using a combination of Hα, Paα, and Brα line ratios is an excellent method of identifying the youngest, most embedded clusters, which are missing from optically based cluster catalogs, and reach clusters that are $\approx$10 times less massive than the limits of the current radio survey of the Antennae.

Acknowledgments

R.C. and P.G. acknowledge support for program No. JWST-GO-2581, which was provided through a grant from the Space Telescope Science Institute (STScI) under NASA contract NAS5-03127. J.D.S., K.S., S.D., G.D., C.W., and L.H. acknowledge funding support from NASA/ADAP grant 80NSSC21K0851. We thank the anonymous referee for suggestions that improved our manuscript. The data presented in this paper were obtained from the Mikulski Archive for Space Telescopes (MAST) at the STScI. The specific observations analyzed can be accessed via doi:10.17909/k2y4-2z87.

Software: Photutils (L. Bradley et al. 2024), Matplotlib (J. D. Hunter 2007), NumPy (S. van der Walt et al. 2011), Astropy (Astropy Collaboration et al. 2018), SciPy (P. Virtanen et al. 2020), SAOImage DS9 (Smithsonian Astrophysical Observatory 2000), APLpy (T. Robitaille & E. Bressert 2012).

Appendix
Identifying Infrared Counterparts to Radio Sources

Radio sources with a thermal component are likely to be the youngest, most massive clusters forming in the Antennae. In this Appendix, we investigate the infrared counterparts to radio sources in the high-resolution 6 and 4 cm catalog compiled by S. G. Neff & J. S. Ulvestad (2000), which is the largest, high-resolution catalog of radio sources in the Antennae currently available. H. He et al. (2022) published properties for a subset of these sources, which are identified at 100, 200, and 345 GHz (from ALMA observations) from their cold dust emission.

Typically, objects with a spectral index α, defined as $S_\nu \propto \nu^\alpha$, with $\alpha_{6-4\mathrm{cm}} \gtrsim -0.4$ are more likely to have a thermal component and hence to be an embedded star cluster, whereas nonthermal sources ($\alpha_{6-4\mathrm{cm}} < -0.4$) are typically supernova remnants. In Table 3, we compile the coordinates, 6 cm flux, and spectral index (if available) for the 19 sources brighter than 200 μJy from S. G. Neff & J. S. Ulvestad (2000). B. C. Whitmore & Q. Zhang (2002) previously found that $\sim$85% (11/13) of the bright, thermal radio sources in the S. G. Neff & J. S. Ulvestad (2000) catalog can be detected in the HST *I*-band image, but did not study the objects individually or in the infrared.

Figure 14 shows $8'' \times 8''$ regions around each of the bright radio sources, including the southern and northern nuclei (regions 1-2 and 7-8), WS80 (2-1), and its neighbor (2-6). The color images are created from the 0.55 μm image (blue), 1.5 μm (green), and continuum-subtracted Paα (red). The green cross shows the source coordinates from S. G. Neff & J. S. Ulvestad (2000). The circles in each stamp have radii of $0\farcs4$ and $0\farcs8$, corresponding to the 1σ and 2σ radio positional uncertainties, respectively. The source identifiers correspond to those in Table 3. Three of these radio sources (2-2, 4-5, and 6-1) have spectral indices $\alpha < -0.4$, which may indicate they are dominated by nonthermal emission, although with only two measurements, the published α values should be viewed with some caution. Eight other sources do not have published spectral indices at all. Below is our summary of infrared counterparts to each radio source listed in the Table.

1. *Clusters with high extinction*. In addition to WS80 (2-1), radio sources 1-3 and 4A-6 have Paα emission and high Brα/Hα and Paα/Hα flux ratios, and high $A_V \gtrsim 5$ mag from our SED fitting. These three sources are fainter at 1.5 μm than at longer wavelengths and are included in our embedded cluster catalog.
2. *Clusters with moderate extinction*. WS80's neighbor (2-6) and radio source 6-1 have Paα emission and moderate Paα/Hα flux ratios. Both are included in our embedded cluster catalog, have best-fit extinction $A_V \approx 3$ mag, and are visible at all infrared and optical wavelengths covered by our images. Despite the low published spectral index of $\alpha = -0.65$, which suggests that source 6-1 might be nonthermal, this radio source is clearly associated with a young star cluster.
3. *Clusters with little extinction*. Radio sources 4-2A and 8-4 both have Paα emission but low Brα/Hα and Paα/Hα flux ratios. They have counterparts that are extended and bright at optical wavelengths, and were included in the HST-based cluster catalog of B. C. Whitmore et al. (2010). The radio emission is from very young clusters with little extinction.

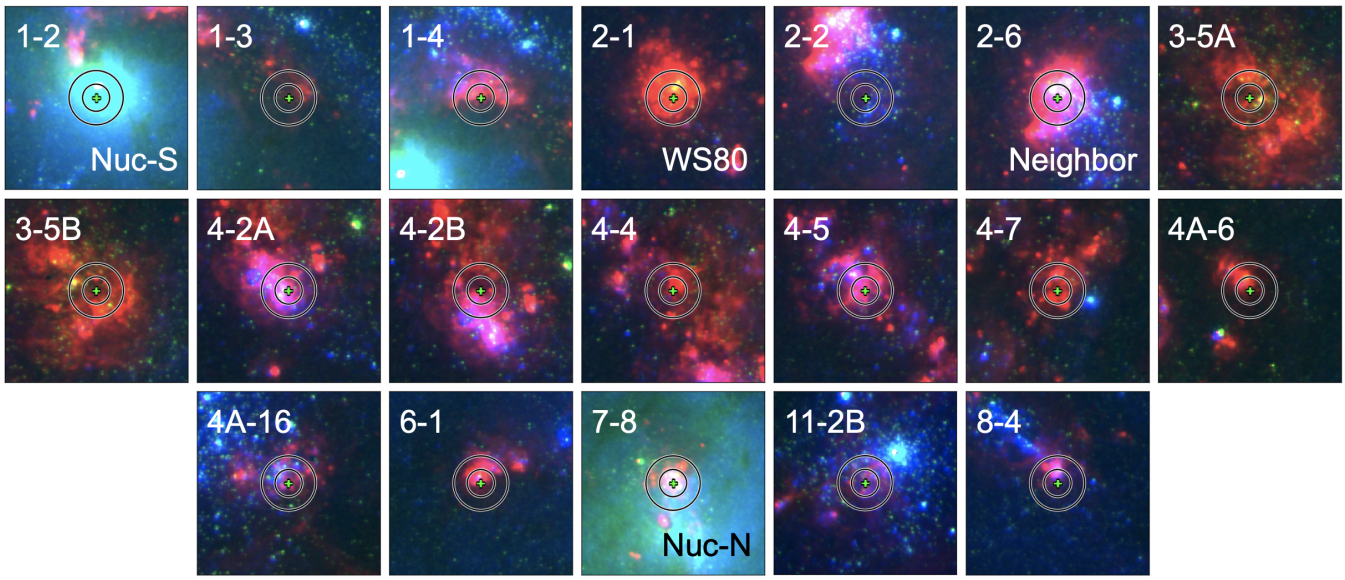

Figure 14. Postage stamps of bright radio sources in V-F150-cont subPaα color image. The two nuclei (sources #1 and #17) and WS80 (source #4) are identified. The green cross shows the radio source location, which has a positional uncertainty of $\approx 0\farcs4$, represented by the small circle. Large circle has a radius of $0\farcs8$.

Table 3
Infrared Counterparts to Bright 6 cm Radio Sources

Region Name	R.A. (J2000)	Decl. (J2000)	6 cm Flux (μJy)	Spectral Index (α)	Notes
1-2	12:01:53.52	−18:53:10.5	513 ± 11	⋯	Nucleus-S
1-3	12:01:53.12	−18:53:09.7	303 ± 11	+ 0.38	bright Paα source, possible match with embedded #4
1-4	12:01:53.35	−18:53:07.9	365 ± 21	−0.20	bright, Paα source
2-1	12:01:54.96	−18:53:06.1	5161 ± 21	−0.26	WS80, brightest Paα source, embedded #9, He22 #1
2-2	12:01:54.52	−18:53:05.4	241 ± 31	−0.51	nonthermal, no Paα source
2-6	12:01:54.58	−18:53:03.4	2257 ± 20	⋯	WS80 neighbor, bright Paα source, embedded #13, He22 #2
3-5A	12:01:54.78	−18:52:51.1	1121 ± 19	⋯	Firecracker region, Paα shell, no counterpart
3-5B	12:01:54.71	−18:52:51.4	2291 ± 49	⋯	Firecracker region, Paα shell, no counterpart
4-2A	12:01:55.34	−18:52:49.2	1215 ± 25	⋯	bright Paα, optical-NIR continuum source
4-2B	12:01:55.38	−18:52:48.0	493 ± 17	⋯	Paα shell, no obvious counterpart, He22 #6
4-4	12:01:55.47	−18:52:45.9	744 ± 11	−0.16	Paα source, no 3.3 μm, He22 #7
4-5	12:01:55.71	−18:52:42.8	243 ± 11	−0.74	nonthermal, Paα shell, no counterpart
4-7	12:01:55:14	−18:52:40.6	616 ± 25	⋯	Paα shell, no counterpart, He22 #8
4A-6	12:01:54.74	−18:52:31.7	341 ± 11	−0.36	bright Paα source embedded #30, He22 #9
4A-16	12:01:55.41	−18:52:24.3	262 ± 27	⋯	Paα shell, no counterpart
6-1	12:01:54.58	−18:51:56.7	493 ± 23	−0.65	bright Paα source, embedded #35, He22 #13
7-8	12:01:53.02	−18:52:02.3	1354 ± 23	⋯	Nucleus-N
11-2B	12:01:50.45	−18:52:13.1	355 ± 29	⋯	Paα shell, no counterpart
8-4	12:01:52.13	−18:52:21.1	198 ± 11	0.18	bright Paα, optical-NIR continuum source

Note. Region names and positions of radio sources with 6 cm flux measurements greater than $\approx$200 μJy are from the catalog of S. G. Neff & J. S. Ulvestad (2000).

4. *Nonthermal*. Source 2-2 has no obvious Paα emission, and source 4-5 shows diffuse Paα with a shell morphology. The spectral indices of these sources suggest they are dominated by nonthermal emission.
5. *No obvious counterpart*. We do not find an obvious peaked infrared source that could be a potential counterpart to radio sources 1-4, 3-5A, 3-5B, 4-2B, 4-4, 4-7, 4A-16, or 11-2B. Most of these have a partial Paα shell near the radio position. Sources 1-4 and 4-4 have a spectral index that suggests they have a thermal component, while the rest do not have published spectral indices.
6. *South and north galaxy nuclei*. The nuclei of the south and north galaxies are radio sources 1-2 and 7-8, respectively.

The bright 6 cm radio sources in the Antennae appear to be somewhat heterogeneous in nature and include very young star clusters with a range of extinction, including some of the most highly extinguished sources in our embedded cluster sample. Most of the bright 6 cm sources, however, are likely nonthermal and not associated with a stellar cluster.

ORCID iDs

Rupali Chandar https://orcid.org/0000-0003-0085-4623
Miranda Caputo https://orcid.org/0000-0002-2957-3924
Paul Goudfrooij https://orcid.org/0000-0002-5728-1427
Sean T. Linden https://orcid.org/0000-0002-1000-6081
Angus Mok https://orcid.org/0000-0001-7413-7534

Cory Whitcomb https://orcid.org/0000-0003-2093-4452
Grant Donnelly https://orcid.org/0009-0001-6065-0414
Florent Renaud https://orcid.org/0000-0001-5073-2267
John-David T. Smith https://orcid.org/0000-0003-1545-5078
Alberto Bolatto https://orcid.org/0000-0002-5480-5686
Danny A. Dale https://orcid.org/0000-0002-5782-9093
Sara Duval https://orcid.org/0000-0003-0014-0508
Lindsey Hands https://orcid.org/0009-0005-0750-2956
Ralf Klessen https://orcid.org/0000-0002-0560-3172
Caroline Kuczek https://orcid.org/0009-0001-3989-1731
Karin Sandstrom https://orcid.org/0000-0002-4378-8534
Eva Schinnerer https://orcid.org/0000-0002-3933-7677
Fabian Walter https://orcid.org/0000-0003-4793-7880

References

Adamo, A., Bradley, L. D., Vanzella, E., et al. 2024, Natur, 632, 513
Adamo, A., Hollyhead, K., Messa, M., et al. 2020, MNRAS, 499, 3267
Astropy Collaboration, Price-Whelan, A. M., Sipőcz, B. M., et al. 2018, AJ, 156, 123
Aversa, A. G., Johnson, K. E., Brogan, C. L., Goss, W. M., & Pisano, D. J. 2011, AJ, 141, 125
Barnes, A. T., Watkins, E. J., Meidt, S. E., et al. 2023, ApJL, 944, L22
Bik, A., Lamers, H. J. G. L. M., Bastian, N., Panagia, N., & Romaniello, M. 2003, A&A, 397, 473
Bradley, L., Sipőcz, B., Robitaille, T., et al. 2024, astropy/photutils: v2.0.2, Zenodo, doi:10.5281/zenodo.13989456
Brandl, B. R., Martín-Hernández, N. L., Schaerer, D., Rosenberg, M., & van der Werf, P. P. 2012, A&A, 543, A61
Brandl, B. R., Snijders, L., den Brok, M., et al. 2009, ApJ, 699, 1982
Bressan, A., Marigo, P., Girardi, L., et al. 2012, MNRAS, 427, 127
Calzetti, D., Armus, L., Bohlin, R. C., et al. 2000, ApJ, 533, 682
Calzetti, D., Wu, S.-Y., Hong, S., et al. 2010, ApJ, 714, 1256
Capriotti, E. R., & Hawley, S. L. 1996, ApJ, 464, 765
Chandar, R., Caputo, M., Mok, A., et al. 2023, ApJ, 949, 116
Chandar, R., Whitmore, B. C., Dinino, D., et al. 2016, ApJ, 824, 71
Claeyssens, A., Adamo, A., Richard, J., et al. 2023, MNRAS, 520, 2180
Conroy, C., Gunn, J. E., & White, M. 2009, ApJ, 699, 486
Conroy, C., White, M., & Gunn, J. E. 2010, ApJ, 708, 58
De Lucia, G., Kruijssen, J. M. D., Trujillo-Gomez, S., Hirschmann, M., & Xie, L. 2024, MNRAS, 530, 2760
Donnelly, G. P., Whitcomb, C. M., Hands, L., et al. 2025, arXiv:2512.12434
Elmegreen, B. G. 2010, ApJL, 712, L184
Emig, K. L., Bolatto, A. D., Leroy, A. K., et al. 2020, ApJ, 903, 50
Fabbiano, G., Zezas, A., & Murray, S. S. 2001, ApJ, 554, 1035
Fall, S. M., Chandar, R., & Whitmore, B. C. 2005, ApJL, 631, L133
Fall, S. M., & Rees, M. J. 1977, MNRAS, 181, 37P
Fall, S. M., & Zhang, Q. 2001, ApJ, 561, 751
Finn, M. K., Johnson, K. E., Brogan, C. L., et al. 2019, ApJ, 874, 120
Gao, Y., Lo, K. Y., Lee, S. W., & Lee, T. H. 2001, ApJ, 548, 172
Gilbert, A. M., & Graham, J. R. 2007, ApJ, 668, 168
Gilbert, A. M., Graham, J. R., McLean, I. S., et al. 2000, ApJL, 533, L57
Gordon, K. D., Clayton, G. C., Decleir, M., et al. 2023, ApJ, 950, 86
Goudfrooij, P., & Fall, S. M. 2016, ApJ, 833, 8
Goudfrooij, P., Strader, J., Brenneman, L., et al. 2003, MNRAS, 343, 665
Graham, G. B., Dale, D. A., Smith, C. L., et al. 2025, AJ, 170, 340
Gregg, B., Calzetti, D., Adamo, A., et al. 2024, ApJ, 971, 115
Guillard, P., Boulanger, F., Pineau des Forêts, G., et al. 2012, ApJ, 749, 158
Haas, M., Chini, R., & Klaas, U. 2005, A&A, 433, L17
He, H., Wilson, C., Brunetti, N., et al. 2022, ApJ, 928, 57
Herrera, C. N., & Boulanger, F. 2017, A&A, 600, A139
Howard, C., Pudritz, R., & Klessen, R. 2017, ApJ, 834, 40
Hummer, D. G., & Storey, P. J. 1987, MNRAS, 224, 801
Hunter, J. D. 2007, CSE, 9, 90
Jog, C. J., & Solomon, P. M. 1992, ApJ, 387, 152
Johnson, B., Foreman-Mackey, D., Sick, J., et al. 2024, dfm/python-fsps: v0.4.7, Zenodo, doi:10.5281/zenodo.12447779
Johnson, K. E., Hunt, L. K., & Reines, A. E. 2009, AJ, 137, 3788
Johnson, K. E., Indebetouw, R., Watson, C., & Kobulnicky, H. A. 2004, AJ, 128, 610
Johnson, K. E., & Kobulnicky, H. A. 2003, ApJ, 597, 923
Johnson, K. E., Kobulnicky, H. A., Massey, P., & Conti, P. S. 2001, ApJ, 559, 864
Johnson, K. E., Leroy, A. K., Indebetouw, R., et al. 2015, ApJ, 806, 35
Kavelaars, J. J., & Hanes, D. A. 1997, MNRAS, 285, L31
Kepley, A. A., Reines, A. E., Johnson, K. E., & Walker, L. M. 2014, AJ, 147, 43
Kim, J., Chevance, M., Kruijssen, J. M. D., et al. 2021, MNRAS, 504, 487
Klaas, U., Nielbock, M., Haas, M., Krause, O., & Schreiber, J. 2010, A&A, 518, L44
Knutas, A., Adamo, A., Pedrini, A., et al. 2025, ApJ, 993, 13
Kobulnicky, H. A., & Johnson, K. E. 1999, ApJ, 527, 154
Kroupa, P. 2001, MNRAS, 322, 231
Kunze, D., Rigopoulou, D., Lutz, D., et al. 1996, A&A, 315, L101
Lai, T. S. Y., Armus, L., Bianchin, M., et al. 2023, ApJL, 957, L26
Li, H., Gnedin, O. Y., Gnedin, N. Y., et al. 2017, ApJ, 834, 69
Li, H., Vogelsberger, M., Marinacci, F., Sales, L. V., & Torrey, P. 2020, MNRAS, 499, 5862
Linden, S. T., Evans, A. S., Armus, L., et al. 2023, ApJL, 944, L55
Maji, M., Zhu, Q., Li, Y., et al. 2017, ApJ, 844, 108
McCrady, N., & Graham, J. R. 2007, ApJ, 663, 844
Messa, M., Calzetti, D., Adamo, A., et al. 2021, ApJ, 909, 121
Messa, M., Dessauges-Zavadsky, M., Adamo, A., Richard, J., & Claeyssens, A. 2024, MNRAS, 529, 2162
Miller, B. W., Whitmore, B. C., Schweizer, F., & Fall, S. M. 1997, AJ, 114, 2381
Mirabel, I. F., Vigroux, L., Charmandaris, V., et al. 1998, A&A, 333, L1
Mok, A., Chandar, R., & Fall, S. M. 2019, ApJ, 872, 93
Mowla, L., Iyer, K. G., Desprez, G., et al. 2022, ApJL, 937, L35
Murphy, E. J., Condon, J. J., Schinnerer, E., et al. 2011, ApJ, 737, 67
Neff, S. G., & Ulvestad, J. S. 2000, AJ, 120, 670
Nguyen, C. T., Costa, G., Girardi, L., et al. 2022, A&A, 665, A126
Ogle, P., Boulanger, F., Guillard, P., et al. 2010, ApJ, 724, 1193
Peng, Y.-j., Lilly, S. J., Kovač, K., et al. 2010, ApJ, 721, 193
Ramambason, L., Chevance, M., Kim, J., et al. 2026, A&A, 706, A186
Renaud, F., Bournaud, F., & Duc, P.-A. 2015, MNRAS, 446, 2038
Riess, A. G., Macri, L., Casertano, S., et al. 2011, ApJ, 730, 119
Robitaille, T., & Bressert, E. 2012, APLpy: Astronomical Plotting Library in Python, Astrophysics Source Code Library, ascl:1208.017
Rodríguez, M. J., Lee, J. C., Indebetouw, R., et al. 2025, ApJ, 983, 137
Rodríguez, M. J., Lee, J. C., Whitmore, B. C., et al. 2023, ApJL, 944, L26
Rosolowsky, E. 2005, PASP, 117, 1403
Rubin, V. C., Ford, W., Kent, J., & D'Odorico, S. 1970, ApJ, 160, 801
Sánchez-Blázquez, P., Gorgas, J., Cardiel, N., & González, J. J. 2006, A&A, 457, 809
Schweizer, F., & Seitzer, P. 2007, AJ, 133, 2132
Senchyna, P., Plat, A., Stark, D. P., et al. 2024, ApJ, 966, 92
Smith, J. D. T., Draine, B. T., Dale, D. A., et al. 2007, ApJ, 656, 770
Smithsonian Astrophysical Observatory 2000, SAOImage DS9: A utility for displaying astronomical images in the X11 window environment, Astrophysics Source Code Library, ascl:0003.002
Stanford, S. A., Sargent, A. I., Sanders, D. B., & Scoville, N. Z. 1990, ApJ, 349, 492
Thilker, D. A., Whitmore, B. C., Lee, J. C., et al. 2022, MNRAS, 509, 4094
Tsuge, K., Tachihara, K., Fukui, Y., et al. 2021, PASJ, 73, 417
van der Walt, S., Colbert, S. C., & Varoquaux, G. 2011, CSE, 13, 22
Vanzella, E., Castellano, M., Bergamini, P., et al. 2022, A&A, 659, A2
Vanzella, E., Loiacono, F., Bergamini, P., et al. 2023, A&A, 678, A173
Vazdekis, A., Koleva, M., Ricciardelli, E., Röck, B., & Falcón-Barroso, J. 2016, MNRAS, 463, 3409
Vazdekis, A., Sánchez-Blázquez, P., Falcón-Barroso, J., et al. 2010, MNRAS, 404, 1639
Virtanen, P., Gommers, R., Oliphant, T. E., et al. 2020, NatMe, 17, 261
Whelan, D. G., Johnson, K. E., Whitney, B. A., Indebetouw, R., & Wood, K. 2011, ApJ, 729, 111
Whitaker, K. E., Cutler, S. E., Chandar, R., et al. 2026, ApJ, 1001, 107
Whitcomb, C. M., Sandstrom, K., Leroy, A., & Smith, J.-D. T. 2023, ApJ, 948, 88
Whitmore, B. C., Brogan, C., Chandar, R., et al. 2014, ApJ, 795, 156
Whitmore, B. C., Chandar, R., Schweizer, F., et al. 2010, AJ, 140, 75
Whitmore, B. C., & Schweizer, F. 1995, AJ, 109, 960
Whitmore, B. C., & Zhang, Q. 2002, AJ, 124, 1418
Whitmore, B. C., Zhang, Q., Leitherer, C., et al. 1999, AJ, 118, 1551
Wilson, C. D., Scoville, N., Madden, S. C., & Charmandaris, V. 2003, ApJ, 599, 1049
Zhang, Q., & Fall, S. M. 1999, ApJL, 527, L81